

JGR Space Physics

RESEARCH ARTICLE

10.1029/2020JA029080

Special Section:

Geospace multi-point observations in Van Allen Probes and Arase era

Key Points:

- Conjugate measurements of an equatorward detachment of the auroral arc from the main oval and the Arase satellite in the inner magnetosphere
- Equatorward detachment of the auroral arc coincided with a localized enhancement of electrons of energies ~ 0.1 – 2 keV deeper down to $L \sim 4.3$ – 4.5
- BATS-R-US–CIMI model successfully reproduced the enhancement of lower-energy electrons (~ 8 – 40 keV) at a lower radial distance ($R < 4$)

Supporting Information:

Supporting Information may be found in the online version of this article.

Correspondence to:

S. Yadav,
sneha.yadav84@gmail.com


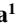





















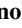
Citation:

Yadav, S., Shiokawa, K., Oyama, S., Inaba, Y., Takahashi, N., Seki, K., et al. (2021). Study of an equatorward detachment of auroral arc from the oval using ground-space observations and the BATS-R-US–CIMI model. *Journal of Geophysical Research: Space Physics*, 126, e2020JA029080. <https://doi.org/10.1029/2020JA029080>

Received 25 DEC 2020

Accepted 12 NOV 2021

Study of an Equatorward Detachment of Auroral Arc From the Oval Using Ground-Space Observations and the BATS-R-US–CIMI Model

Sneha Yadav¹ , K. Shiokawa¹ , S. Oyama^{1,2} , Y. Inaba¹ , N. Takahashi^{3,4} , K. Seki³ , K. Keika³ , Tzu-Fang Chang⁵, S. W. Y. Tam⁵, B.-J. Wang⁶, Y. Kazama⁶ , S.-Y. Wang⁶ , K. Asamura⁷ , S. Kasahara³ , S. Yokota⁸ , T. Hori¹ , Y. Kasaba⁹ , F. Tsuchiya⁹ , A. Kumamoto⁹ , M. Shoji¹ , Y. Kasahara¹⁰ , A. Matsuoka^{7,11} , S. Matsuda^{7,10} , C.-W. Jun¹ , S. Imajo^{1,11} , Y. Miyoshi¹ , and I. Shinohara⁷ 

¹Institute for Space-Earth Environmental Research, Nagoya University, Nagoya, Japan, ²National Institute of Polar Research, Tokyo, Japan, ³Graduate School of Science, University of Tokyo, Tokyo, Japan, ⁴National Institute of Information and Communications Technology, Koganei, Japan, ⁵National Cheng Kung University, Tainan, Taiwan, ROC, ⁶Academia Sinica Institute of Astronomy and Astrophysics, Taipei, Taiwan, ⁷Institute of Space and Astronautical Science, Japan Aerospace Exploration Agency, Sagami, Japan, ⁸Graduate School of Science, Osaka University, Toyonaka, Japan, ⁹Tohoku University, Sendai, Japan, ¹⁰Graduate School of Natural Science and Technology, Kanazawa University, Kakuma, Kanazawa, Japan, ¹¹Graduate School of Science, Kyoto University, Kyoto, Japan

Abstract We present observations of an equatorward detachment of the auroral arc from the main oval and magnetically conjugate measurements made by the Arase satellite in the inner magnetosphere. The all-sky imager at Gakona (magnetic latitude = 63.6°N), Alaska, shows the detachment of the auroral arc in both red and green lines at local midnight (~ 0130 – 0230 MLT) on 30 March 2017. The electron density derived from the Arase in-situ observations shows that this arc occurred outside the plasmopause. At the arc crossing, the electron flux of energies ~ 0.1 – 2 keV is found to be locally enhanced at $L \sim 4.3$ – 4.5 . We estimated auroral intensities for both red and green lines by using the Arase low-energy (0.1 – 19 keV) electron flux data. The peak latitude of the estimated intensity shows reasonably good correspondence with the observed intensity mapped at the ionospheric footprints of the Arase satellite. These findings indicate that the observed arc detachment at Gakona was associated with the localized enhancement of low-energy electrons (~ 0.1 – 2 keV) at the inner edge of the electron plasma sheet. Further, we employ the simulation results of the Community Coordinated Modeling Center (CCMC), the BATS-R-US–CIMI 3-D MHD code to understand the conditions in the inner magnetosphere around the time of detachment. Although the simulation could not reproduce the lower-energy component responsible for the arc detachment, it successfully reproduced two earthward convection events at the lower radial distance (R) ($R \leq 4$) around the time of arc detachment and the features of enhanced convection in similarity with the observations.

1. Introduction

The solar wind energy and its complex interaction with the magnetosphere powers the vibrant aurora in the Earth's upper atmosphere. The aurora is an optical emission produced by the energetic electrons precipitating along the geomagnetic field, eventually collide and excite particles in the upper atmosphere that, in turn, emit photons (e.g., Jones, 1974). The diverse processes occurring in different regions of the magnetosphere cause the formation of aurora in various forms.

An auroral arc is defined as a curtain-shaped optical emission aligned along the geomagnetic east-west direction in the upper atmosphere (e.g., Karlsson et al., 2020, for a review). Different types of arcs correspond to different regions of the Earth's magnetosphere and diverse processes that occur in the region. Therefore, these arcs serve as a diagnostic tool for investigating the large-scale processes occurring in the magnetosphere and their association with the ionosphere.

During geomagnetic storm periods, the interaction of the inner edge of the ring current with the contracted plasmasphere leads to the formation of the stable auroral red (SAR) arc at subauroral latitudes. SAR arc emissions are caused by the thermal excitation of oxygen atoms due to the heat conduction along geomagnetic field lines connecting the ionosphere with the plasmasphere, driven by the storm time ring current (Cole, 1965). Recently,

a new type of transient red arc has been reported to be emerged at 68° MLat associated with pseudo breakup, probably representing the moment of SAR arc birth (Oyama et al., 2020). A spectacular emission feature known as strong thermal emission velocity enhancement (STEVE) has also grasped the attention of the space physics community in recent years (MacDonald et al., 2018). STEVE is a visible mauve or purple color arc that is approximately east-west aligned, extending to thousands of kilometers in the meridional direction. Both SAR arc (Takagi et al., 2018) and STEVE (Yadav et al., 2021) have shown to be detached from the main auroral oval.

The term "detached arcs" was introduced by Anger et al. (1978) to describe the arc-like auroral features equatorward of the auroral oval observed in the afternoon sector by the Isis 2 satellite scanning photometer, also known as the "afternoon detached auroral arcs." These detached arcs showed some similarities to SAR arcs in terms of their location and occurrence (both observed in the trough region and subsiding substorm activity) but were completely different spectroscopically as they were observed in 391.4 nm (N_2^+) and 557.7 nm with no emission enhancement in 630.0 nm. Moshupi et al. (1979) suggested that the source for the trough region auroras are plasma sheet particles left behind by a poleward retreat of the auroral oval. Later, particle observations made by the energetic particle detector onboard Isis 2 showed that these detached arcs are formed at the feet of field lines having a trapped population of electrons $1 \leq E_e \leq 10$ keV as well as usual higher-energy radiation belt particles. It was also suggested that the pitch angles of the residual plasma sheet population would be scattered into the loss cone by electron cyclotron resonance in the cold plasma region outside of the plasmopause (Wallis et al., 1979). In addition to the detached arcs caused by electron precipitation, detached proton arcs have also been observed in the subauroral region (Zhou et al., 2021 and reference therein). Detached subauroral proton arcs have been shown to be formed by the precipitation of high-energy ions caused by the interactions of EMIC waves with ring current ions (e.g., Sakaguchi et al., 2008; Zhou et al., 2021). A review on these detached auroral features from the auroral oval is provided by Frey (2007). Although observed in the subauroral region, the detached arc we are presenting in this study is different from the above arcs because it is observed in the midnight sector with emissions in both 630.0 nm and 557.7 nm. The detachment mechanism of midnight detached arcs and their association with the inner magnetosphere is still not known.

The emergence of satellite measurements in the magnetosphere has paved the way to study the source region of auroral features in the magnetosphere using a space-ground conjunction event. For example, the observations from Defense Meteorological Satellite Program (DMSP) revealed that auroral arc corresponds to an electron inverted-V structure near the equatorward edge of the electron precipitation region, suggesting the pseudo breakup of the auroral substorm occurred in the inner part of the plasma sheet (Yago et al., 2005). By using the Active Magnetosphere and Planetary Electrodynamics Response Experiment (AMPERE) and the Van Allen Probes B (RBSP-B) in the inner magnetosphere (L values of ~ 5.0 – 5.6), Motoba et al. (2015) suggested that the pre-midnight arc is connected to highly localized pressure gradients embedded in the near tail region-2 source region via the local upward field-aligned current. Recently, Shiokawa et al. (2020) reported the first observation of the source plasma features of auroral arcs and diffuse auroras in the inner magnetosphere by the Arase satellite. They observed the bidirectional field-aligned electrons with structured energy-time spectra in the source region of auroral arcs. By using the Arase satellite, Inaba et al. (2020) investigated the magnetospheric source region of the SAR arc and reported that heating of plasmaspheric electrons and multispecies ions via Coulomb collision with ring-current ions is indeed the most plausible mechanism for the SAR arc generation.

The coordinated ground- and space-based measurement at the time of arc detachment might shed some light on the series of processes occurring in the magnetosphere that causes the detachment of arc from the main auroral oval. However, such measurements are extremely limited because of the rarity of satellite crossing exactly at the time of arc detachment and other difficulties such as clear sky. In addition to the conjugate measurements, the numerical simulation might also play an important role in explaining the underlying physical mechanisms in the inner magnetosphere and their linkage with the ionosphere.

In this study, we present a space-ground conjunction event of an equatorward detachment of the auroral arc that occurred on 30 March 2017. This event was exclusive due to the crossing of the Arase satellite in the inner magnetosphere over the field of view of the all-sky imager operating at Gakona and therefore has been used previously for the space-ground conjunction event analysis by Ozaki et al. (2019) and Hosokawa et al. (2020). In the present study, the ionospheric footprints of the Arase satellite crossed the region around the time of arc detachment, providing a unique opportunity to investigate the magnetospheric linkage of the arc detachment. Through the ground-based all-sky imager (ASI) observations of aurora in red and green lines together with

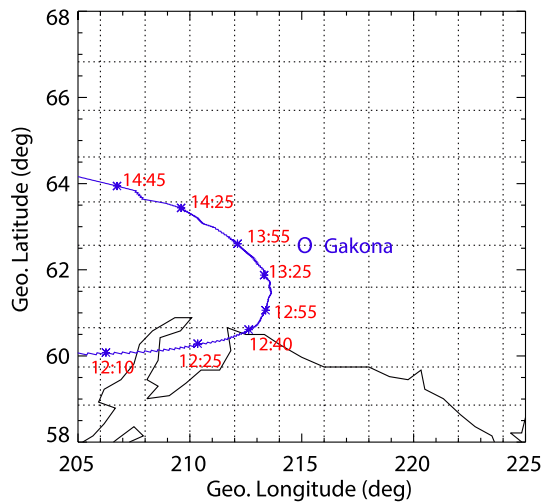


Figure 1. Map displaying the crossing of the Arase satellite over the region covered by the all-sky imager at Gakona. The location of Gakona is depicted by a blue circle. The path of the ionospheric footprint of the Arase satellite mapped to an altitude of 300 km is indicated by the blue curve.

the simultaneous conjugate space-based observations of particle flux, and electric and magnetic field variations, we investigate the connection between source magnetosphere and ionosphere that leads to the detachment of arc in the subauroral region. We extend this study by including simulation results from the BATS-R-US-CIMI (Block-Adaptive-Tree Solar-Wind Roe-Type Upwind Scheme-Comprehensive Inner Magnetosphere-Ionosphere) model to physically interpret the connection between source magnetosphere and ionosphere by comparing simulation and in-situ observations.

2. Database and Methodology

This study is based on three kinds of data sources: ground-based (ASI), space-based (Arase), and simulations.

2.1. Ground-Based Measurements

An OMTI (Optical Mesosphere Thermosphere Imager) (Shiokawa et al., 1999, 2009b) all-sky imager (camera no. 19) has been operating at Gakona (62.4°N, 214.7°E, magnetic latitude: 63.2°N, $L = 4.9$), since 2017, under the PWING project (study of dynamical variation of particles and waves in the inner magnetosphere using ground-based network observations) (Shiokawa et al., 2017). Magnetic midnight for this ASI occurs at 10.7 UT.

This imager has a 180° field-of-view fish-eye lens, five band-pass optical filters including background (572.5 nm), and a thermoelectrically cooled CCD with 1024×1024 pixels. In this work, we have used airglow/auroral images at two wavelengths: OI at 557.7 nm and OI at 630.0 nm with exposure times of 15 sec and 30 sec, respectively. These images are processed with 2×2 binning to increase the signal-to-noise ratio, reducing the image resolution to 512×512 pixels. In order to remove the background continuum emission, we have subtracted the background images. In order to project images onto the geographical latitude/longitude coordinates, it is a prerequisite to assume the emission altitude. In general, for airglow study, an emission height of 250 km is used as a standard height for 630.0 nm (Blanchard et al., 1997). An emission altitude of 400 km has been usually adopted for the monochromatic SAR arc (Roach & Roach, 1963). The mapping altitude of 180–220 km was derived for the discrete red-line arc by using the triangulation method (Jackel et al., 2003). The detached auroral arc in the present study is not monochromatic as emissions are also observed in the green line. Because of this reason, we have assumed an altitude of 300 km for 630.0 nm and 120 km for 557.7 nm to project raw all-sky images onto the geographical latitude/longitude coordinates.

2.2. Space-Based Measurements

The in-situ observations of particles and electric and magnetic fields are obtained by the Exploration of energization and Radiation in Geospace (ERG) satellite, also known as the Arase satellite (Miyoshi et al., 2018a). Launched on 20 December 2016, Arase has an elliptical orbit with a perigee of ~ 400 km and an apogee of $\sim 32,000$ km ($R \sim 6$ RE) (where R is the radial distance and RE is the Earth's radius) with an inclination of $\sim 31^\circ$.

On 30 March 2017, the Arase satellite crossed the field of view of the Gakona ASI at ~ 1200 –1400 UT. Figure 1 shows the region covered by the Gakona ASI along with the path of the ionospheric footprint of the Arase satellite mapped to an altitude of 300 km, calculated by using the Tsyganenko-Sitnov (TS05) model (Tsyganenko & Sitnov, 2005). The model used the solar wind and W-parameters (the database of solar wind characteristics) as an input taken from the TS05 web repository published by N. Tsyganenko. The location of Gakona is marked by a blue circle. The footprint of Arase approaches Gakona from the southwest, remain close to Gakona during 1230–1330 UT and thereafter move in the northwest direction.

In this work, we use the data from the following instruments onboard the Arase: the Low-Energy Particle Experiments-Electron Analyzer (LEP-e) (Kazama et al., 2017), the Medium-Energy Particle Experiments-Electron Analyzer (MEP-e) (Kasahara et al., 2018a), the Medium-Energy Particle Experiments-Ion Mass Analyzer (MEP-i) (Yokota et al., 2017), the Magnetic Field Experiment (MGF) (Matsuoka et al., 2018a), and the Plasma

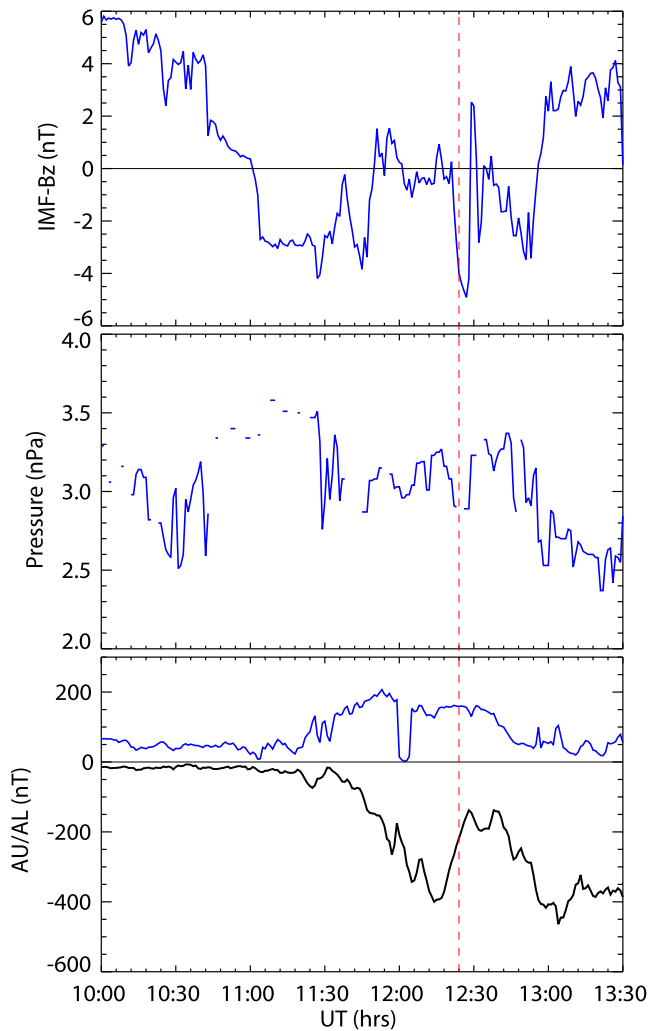


Figure 2. (From top to bottom) Variation of interplanetary magnetic field (IMF)-Bz, solar wind plasma pressure, and AU/AL index on 30 March 2017 at 1000–1330 UT. The dashed line highlights the approximate time of the arc detachment.

Wave Experiment (PWE) (Kasahara et al., 2018b) with the Electric Field Detector (EFD) (Kasaba et al., 2017), the High-Frequency Analyzer (HFA) (Kumamoto et al., 2018), and the Waveform Capture/Onboard Frequency Analyzer (WFC/OFA) (Matsuda et al., 2018). We have used the Space Physics Environment Data Analysis Software (SPEDAS) tool (Angelopoulos et al., 2019) to analyze the Arase satellite data.

2.3. Model Description

We use the Comprehensive Inner-Magnetosphere Ionosphere (CIMI) model with the Block-Adaptive-Tree Solar-Wind Roe-Type Upwind Scheme (BATS-R-US) magnetosphere model available through the Space Weather Modeling Framework (SWMF) (Tóth et al., 2005; 2012). While CIMI represents the inner magnetosphere, the global magnetosphere is represented by BATS-R-US. The coupling of these codes allows us to simulate consistently the inner and outer magnetosphere. The simulation results are provided by the Community Coordinate Modeling Center (CCMC, <http://ccmc.gsfc.nasa.gov>). BATS-R-US is typically configured to solve the ideal MHD equations on a three-dimensional Cartesian grid (Gombosi et al., 2000; Powell et al., 1999). The computational domain of BATS-R-US extends from 32RE upstream to 224RE downstream of the planet and 64RE to the sides in Y and Z directions in the Geocentric Solar Magnetospheric (GSM) coordinates. The grid resolution is 0.15 RE x 0.15 RE x 0.15 RE at the finest. The temporal resolution of output files for MHD parameters is a minute. The CIMI describes the phase-space densities of energetic electrons (1–3,162 keV) and ions (0.1–316 keV) in the inner magnetosphere calculated by solving the bounce-averaged Boltzmann transport equation (Fok et al., 2014). The grid in CIMI is defined by the ionospheric foot point of the field line. The temporal resolution of output files for phase space densities is 5 minutes. The boundary between CIMI and BATS-R-US is defined as the last closed field line (typically about 8–10 RE) while the inner boundary of CIMI is 2.5 RE. The simulation time goes from 1500 UT on 29 March 2017 and runs for 1 day. The simulations used DSCOVR L2 data as an input for solar wind parameters. All solar wind data are interpolated onto a 1-minute cadence.

3. Results

The results have been divided into four subsections. The first subsection deals with the solar wind and geomagnetic conditions during the event of arc detachment. The observations from ground-based ASI at Gakona showing the feature of arc detachment are described in Subsection 3.2. The conjugate measurements of particle flux at different energies and electric and magnetic fields made by the Arase satellite are given in Subsection 3.3. The results obtained by model simulations are described in Subsection 3.4 while Subsection 3.5 provide the details about the estimated auroral intensity based on the low-energy electron flux observed by the Arase satellite.

3.1. Solar Wind and Geomagnetic Conditions

Figure 2 shows the interplanetary magnetic field (IMF) Bz component, solar wind plasma pressure (Psw), AU/AL indices at 1000–1330 UT. The IMF Bz shows two main events of southward orientation, first at ~1100–1150 UT and second at ~1220–1255 UT. While maintaining a northward orientation, IMF Bz shows a decreasing trend during the interval 1000–1100 UT. It turns southward at ~1100 UT and remains dominantly southward during the interval 1100–1150 UT with a maximum negative excursion of about –4 nT. After remaining quiet for around 30 mins (~1150–1220 UT), the IMF Bz abruptly turned southward at 1220 UT. Although it remains mostly southward at ~1220–1255 UT, the IMF Bz shows some fluctuations in terms of rapid turning between southward and

northward directions. The solar wind plasma pressure was also enhanced from ~ 2.5 nPa to 3.5 nPa during the first event of IMF Bz negative excursion. The Psw attains the values of about 2.8–3.3 nPa at the interval 1130–1250 UT and shows a decreasing trend afterwards. The AU/AL indices do not show any considerable change at 1000–1130 UT, which remains close to zero. The negative bay-like structure in AL at ~ 1130 –1225 UT indicates the presence of a substorm-like activity. It is notable that this activity started 30 mins after the southward turning of IMF-Bz. After attaining constant values for about 10 mins (~ 1225 –1235 UT), the AL index shows another bay-like structure at ~ 1235 –1310 UT, indicating the presence of second substorm-like activity. This substorm activity started ~ 15 -mins after the southward turning of IMF Bz at ~ 1220 UT.

In order to check the correspondence between signatures of substorms in the observations (AU/AL) and model simulations, we simulate plasma pressure (Movie S1) and velocity (Vx component) (Movie S2), and the dawn-to-dusk component of the electric field (Ey) (Movie S3) during the interval ~ 1030 –1315 UT. Note that the region around 10 Re is the boundary between BATS-R-US and CIMI, which may cause artificial effects, appeared in terms of a circle-like structure at ~ 10 Re in the global simulations. While AU/AL observations show the substorm signature after 1130 UT, a continuous increase in velocity (both sunward and antisunward) in the tailward side of the Earth is observed after 1030 UT, coinciding with the decreasing trend of IMF Bz. After the southward turning of IMF Bz at 1100 UT, the reconnection develops longitudinally in the Y-direction. Unlike velocity, the simulated pressure shows continuous fluctuations throughout the time duration; however, enhanced pressure in the nightside direction is noticeable at 1120–1150 UT, coinciding with the first substorm. The velocity in the nightside direction also seems to maximize at ~ 1135 –1155 UT. For the second substorm activity as observed in the AU/AL indices at ~ 1235 –1310 UT, both pressure and velocity show random fluctuations with no distinct variation. Although BATS-R-US–CIMI simulate the enhanced nightside activities, particularly for ~ 1130 –1225 UT when the first substorm-like activity occurred in AU/AL, it could not reproduce any distinct variation in both pressure and velocity for the second substorm-like activity observed in the AU/AL indices. It is notable that, for the present case, it is not possible to distinguish the substorm onset timings in the simulations. Further, the comparison between the observed and simulated AU/AL indices (not shown here) showed that although the simulated AU/AL index showed smooth and weak variations from 1130 onwards, it could not reproduce the substorm activity. In the global simulations, the Ey component in the nightside showed significant enhancement from ~ 5 to 15 Re in association with the southward turning of IMF-Bz. The Ey component began to increase gradually after ~ 1030 UT and abruptly after ~ 1110 UT. The Ey component displayed continuously large values at ~ 1115 –1200 UT, exhibiting the values of about ~ 1 –3 mV/m at 5–15 Re in the nightside. After displaying the relatively lower values at ~ 1200 –1215 UT, the Ey again showed an enhancement from ~ 1225 UT, probably in response to the turning of IMF Bz in the southward direction at this time. The enhanced simulated Ey in the inner magnetosphere inside the geosynchronous orbit ($Re < 6$) is also notable. The Ey showed higher values in the midnight to dawn sector as compared to the dusk sector, particularly inside the geosynchronous orbit. The increased values of simulated Ey inside the geosynchronous orbit might indicate the presence of enhanced localized electric fields in the deep injection region.

3.2. Ground-Based Observations of the Auroral arc at Gakona

Figure 3 depicts the North-South (N-S) keogram for both red- and green-line emissions during the interval 1130–1330 UT, constructed by stripping the slices of airglow images at the longitude of Gakona (214.7°E). The strong brightness in the northern part of the keograms indicates the presence of an auroral oval. The auroral oval moves in the equatorward direction after 1130 UT in the red-line keogram. The effect of two substorm activities is also observed in the red-line keogram in terms of enhanced auroral intensities at ~ 1150 –1225 UT and ~ 1230 –1320 UT in the northward part of the keogram. Such feature is not identified in the green-line keogram because of the saturation in the poleward part of the images at latitudes of 63 – 66° . However, in spite of the saturation, the equatorward motion of the auroral oval can be identified in the green line from 1130 UT. In the red-line keogram, a narrow latitudinal structure separates itself from the main auroral oval at ~ 1220 –1225 UT (depicted by dashed line). After separating itself from the main auroral oval, the arc began to move in the equatorward direction. This narrow latitudinal structure, located equatorward of the auroral oval, is known as the auroral arc and the feature of its separation from the main auroral oval is referred to as the detachment of the auroral arc. The process of detachment occurred during the recovery phase of the first substorm. After detachment, this arc shifted equatorward from 62°N to 59°N at 1300 UT, exhibiting a shift of $\sim 3^\circ$. The arc in the red line appeared until the end of observation at 1330 UT. Thus, due to the unavailability of the observations after 1330 UT, the time duration of

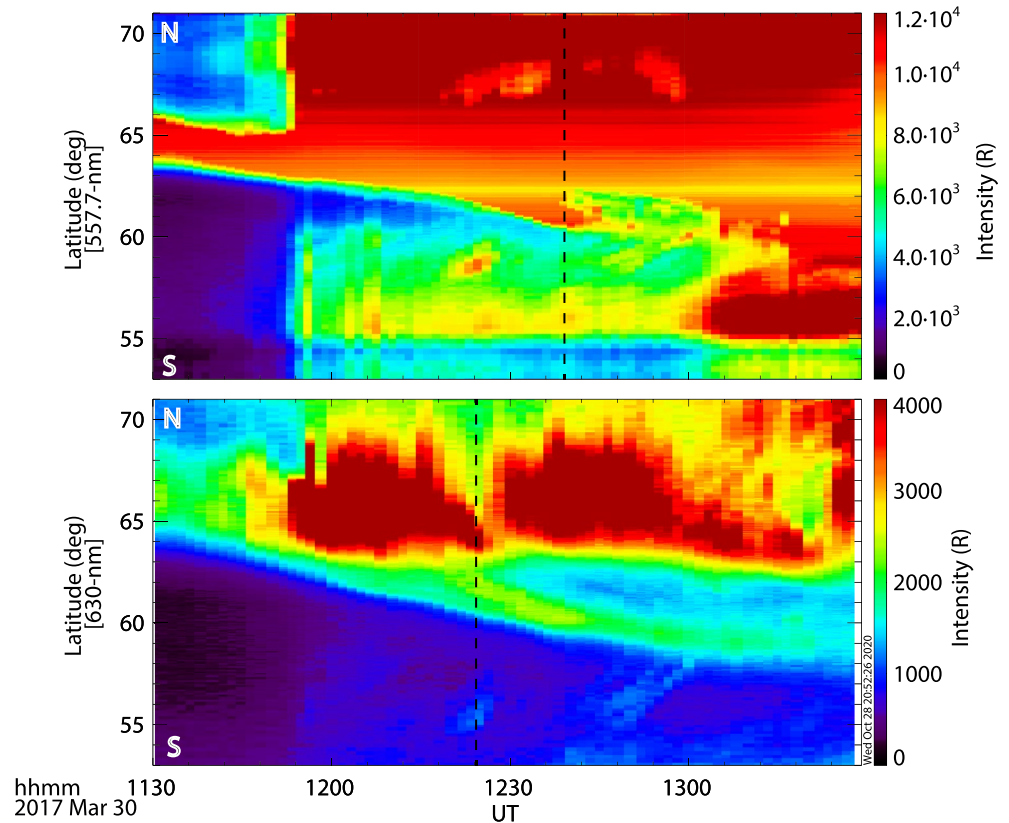


Figure 3. North-South (N-S) keogram for the green (557.7 nm) and red lines (630.0 nm). The intense brightness in the northern part of the keograms represents the auroral oval. The dashed lines highlight the detachment of the auroral arc.

the arc remains unknown. The intense brightness caused by the aurora in the poleward auroral oval leads to the saturation of the images in the green line, causing the formation of artificial structure at $\sim 63\text{--}66^\circ$ in the green-line keogram. In spite of the saturation, the feature of arc detachment is observed in the green line at ~ 1235 UT, which shifted to 60°N at 1300 UT (depicted by the dashed line). The detached arc is also observed in the THEMIS white light imager (not shown) at Gakona (62.4°N ; 214.8°E , magnetic latitude: 63.1°N) and Whitehorse (61°N ; 224.8°E , magnetic latitude: 63.9°N). Although we assume that the arc in the red and green lines is the same, the latitudinal difference of $\sim 1^\circ$ in the red and green lines might be associated with the ambiguity in the assumed emission altitude. Unlike the red-line arc, the arc in the green line appeared until 1300 UT, and thereafter, the bright aurora covers the entire field of view of the camera. The intense emission in the south in the green-line keogram at $1200\text{--}1330$ UT is probably a reflection of the northern auroral emission by a dome that covers the ASI; however, there is also a possibility of contamination from the dawn terminator.

Figure 4 shows the red-line auroral images during the interval $1203\text{--}1250$ UT on 30 March 2017 at Gakona. These images are mapped to geographical coordinates by assuming an emission altitude of 300 km. The ionospheric footprint of the Arase satellite is marked by the black asterisk symbol. The bright emission in the northern part of the images indicates the main auroral oval. Initially, at ~ 1220 UT, the changes at the edge of the auroral oval are observed (indicated by white arrows) as compared to the previous images. At ~ 1224 UT, an arc-like structure begins to develop at 62°N with a low-intensity region at the immediate poleward boundary of the arc. This latitudinally narrow (meridional width of $\sim 1^\circ$) but east-west elongated emission structure, located equatorward of the auroral oval, is known as the auroral arc (highlighted by black arrows) and the phenomenon is referred to as the detachment of the auroral arc from the main auroral oval. Although the detachment of arc is observed at ~ 1224 UT, there is a possibility that the arc might be formed inside the main oval but remained masked by surrounding bright aurorae. After detaching from the auroral oval, the arc becomes wider, shifted equatorward, and observed at $\sim 59^\circ\text{N}$ at 1250 UT, exhibiting a shift of ~ 3 degrees.

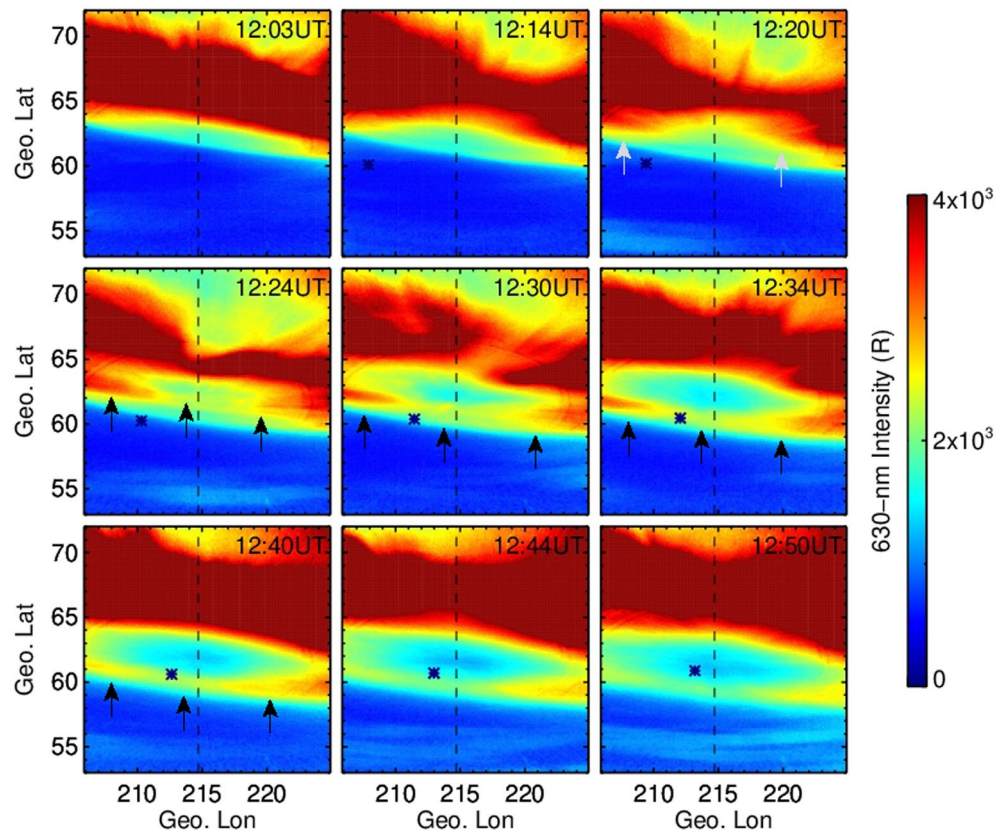


Figure 4. Red-line (630.0 nm) emission airglow/auroral images during the interval 1203–1250 UT on 30 March 2017 at Gakona. The brightness in the northern part of the images indicates the auroral oval. The footprint of the Arase satellite is shown by the black asterisk symbol. White arrows highlight the changes in the shape of the auroral oval before the arc detachment, whereas black arrows indicate the auroral arc.

The ionospheric footprint of the Arase satellite is located at the equatorward boundary of the auroral oval at ~ 1220 UT, moves into the auroral arc at ~ 1230 – 1234 UT, and is seen poleward of the auroral arc after ~ 1244 UT. The overlapping of the Arase ionospheric footprint at the brightened arc during the interval ~ 1225 – 1240 UT indicates that the Arase satellite traversed the region around the time of arc detachment. The feature of arc detachment from the main auroral oval and satellite trajectory over the region covered by ASI can be seen in supplementary Movie S4.

In similarity with Figure 4, the images (1204–1247 UT) in Figure 5 and supplementary Movie S5 show the development and detachment of arc in the green line on 30 March 2017 at Gakona. As already discussed, the processes of arc detachment in the green-line images are not as conspicuous as observed in the red line because of the saturation of images in the poleward direction. The changes in the boundary of the auroral oval, as observed in the red line, cannot be identified in the green line. The presence of arc at $\sim 61^\circ$ N is observed in the images at 1234–1243 UT (highlighted by black arrows). The ionospheric footprint of the Arase satellite at 120 km altitude crossed the arc in the green-line images at 1234–1243 UT.

3.3. Arase Observations

Figure 6 shows the (a) electron density, the energy-time flux spectra (omnidirectional) of (b) low- and (c) medium-energy electrons and (d) medium-energy ions observed by the Arase satellite, and airglow/auroral intensity for (e) red and (f) green lines at the ionospheric footprint of Arase at three different mapping altitudes (200, 300, and 400 km for red line and 100, 120, and 150 km for green line) during 1200–1330 UT on 30 March 2017. The labels below the X-axis in the figure show the location of the Arase satellite with respect to L^* (L^* is the magnetic drift invariant, also known as the Roederer L parameter) (Roederer, 1970), referred to as the L-value here;

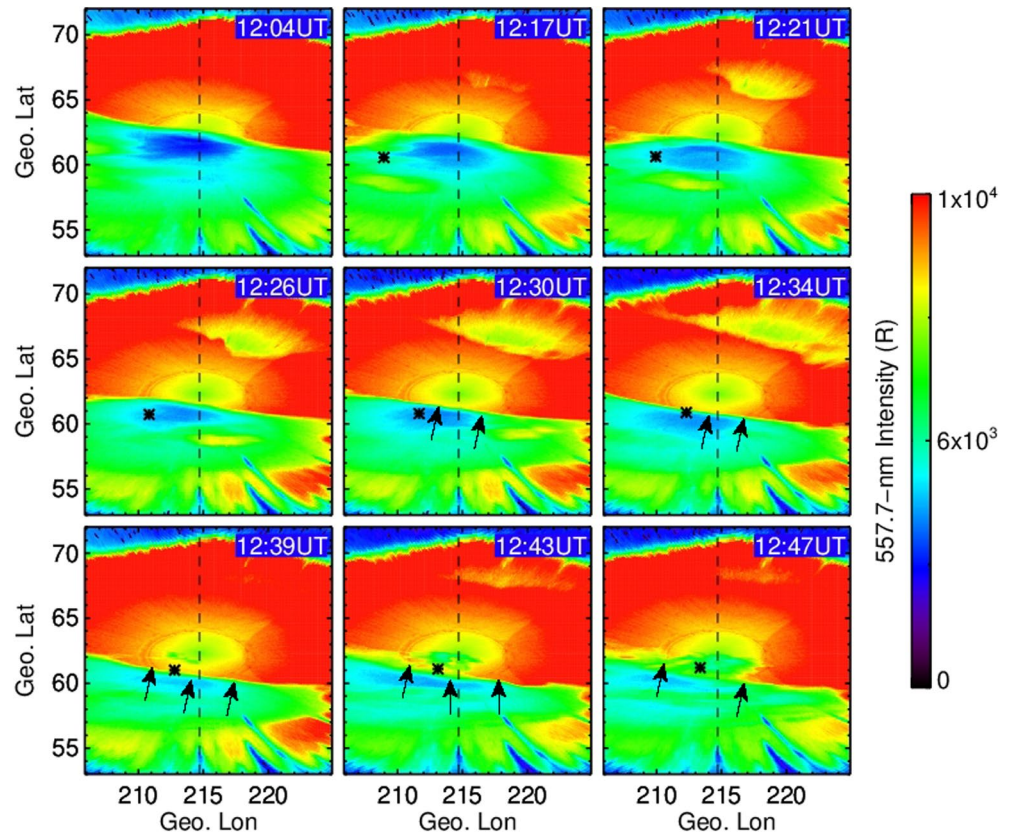


Figure 5. Same as Figure 4 but for the green line (557.7 nm) and during the interval 1204–1247 UT.

magnetic local time (MLT), magnetic latitude (MLAT), and radial distance (R). During the interval 1200–1330 UT, the satellite moved outward from $L = 3.8$ to $L = 5.0$ and was located in the midnight sector (0.4–2.5 MLT) in the southern hemisphere. The electron number density, shown in panel (a), is derived from the upper hybrid resonance (UHR) waves observed by the HFA/PWE onboard the Arase satellite. The periodic data gap in LEPE energy time spectra below 1 keV is associated with the change in observation mode.

We have estimated emission intensities at the ionospheric footprint of the Arase satellite at three different mapping altitudes because of the ambiguities in the assumption of the altitude of the emission layer. At all three mapping altitudes, a significant increase in the emission intensities is observed at ~ 1224 – 1251 UT for both red and green lines, indicating the auroral arc (highlighted by dashed lines). In addition to the emission altitude, the magnetospheric models could also cause the uncertainties of the Arase's ionospheric footprint; therefore, we calculated the ionospheric footprint of the Arase satellite using different models (e.g., IGRF only, T01, T96, and TS05, not shown here). Although with a slight discrepancy in latitude ($\leq 1^\circ$), the arc is observed in all the models. For brevity, in Figure 6 (e) and (f), the emission intensities at the ionospheric footprint of Arase are shown only for TS05. While the emission peak at different mapping altitudes shows a discrepancy in magnitude of ~ 200 Rayleigh (Ry) for the red line, it is observed to be ~ 1500 Ry for the green line. At the time of arc detachment, the auroral intensity for the red line (at 300 km) increases from ~ 600 Ry to ~ 2300 Ry, exhibiting an enhancement of ~ 1700 Ry. This abrupt increase in the intensity represents a spatial pattern of the relative location of the satellite to the arc rather than temporal variation. Similarly, the auroral intensity for the green line (at 120-km) increases from 4500 Ry to 10000 Ry, showing a substantial enhancement of ~ 5500 Ry. A slight difference in latitude ($< 1^\circ$) in the onset and peak emission intensity of the arc at the ionospheric footprints of the Arase satellite at three emission altitudes indicates the ambiguity in mapping.

The electron density (panel a) shows a consistently decreasing trend with a steep decrease at 1220 UT, suggesting a plasmopause crossing at this timing. This indicates that the detachment of arc in the ionosphere occurred at the base of the flux tube that is outside the plasmopause where ambient electron density was around 1–10 electrons/cm³.

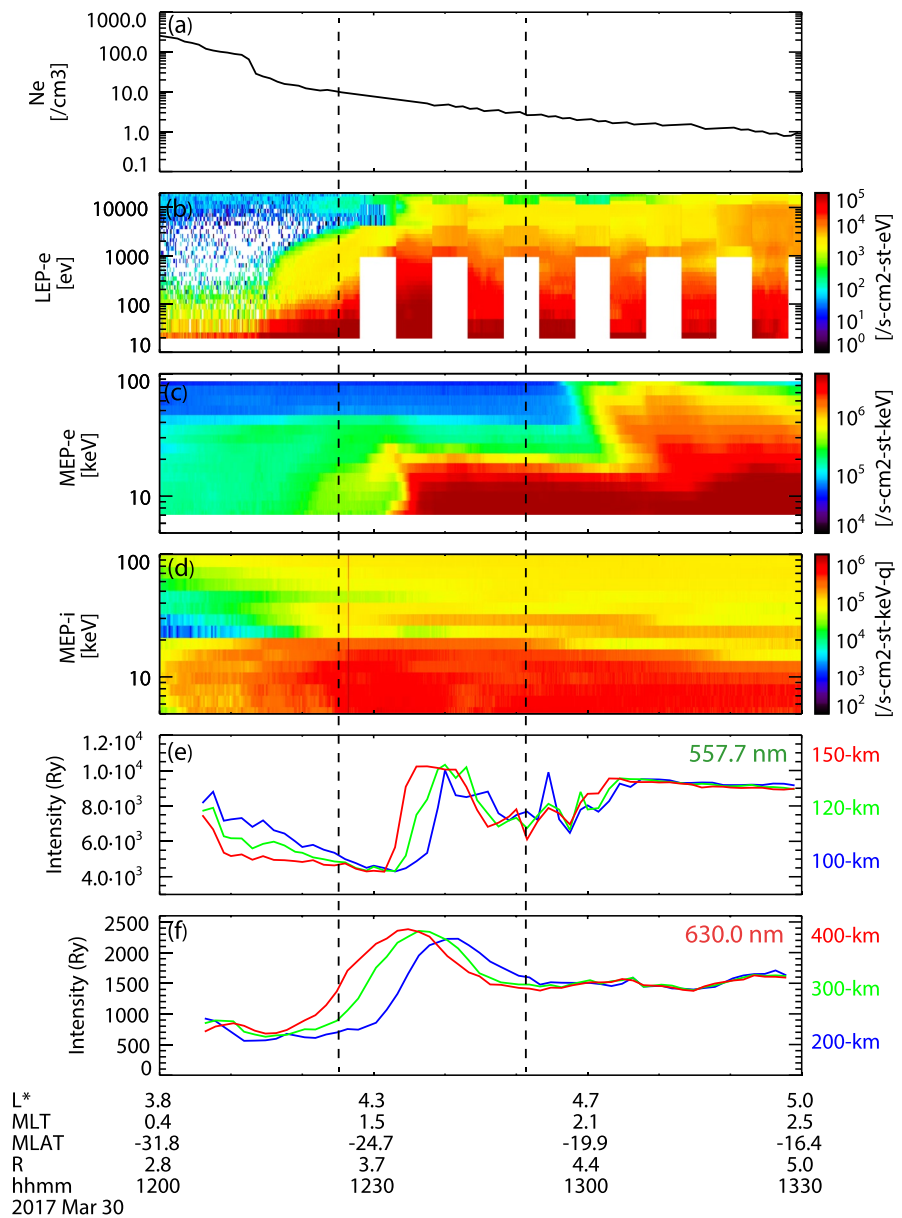


Figure 6. Variation of (a) electron density, (b) low- & (c) medium-energy electron, and (d) medium-energy ion energy-time spectra (omnidirectional) observed by the Arase satellite, and airglow/auroral intensity for (e) red and (f) green line at the ionospheric footprint of the Arase satellite at three different mapping altitudes during 1200–1330 UT on 30 March 2017. The periodic data gap in LEPe energy time spectra below 1 keV is associated with the change in observation mode.

In LEPe energy time (E-t) spectrum (panel b), we can see the electrons of energies <1 keV being penetrated deeper to $L \sim 4.1$ at ~ 1215 UT, indicating the electron plasma sheet. At the inner boundary of the electron plasma sheet, the electrons of energies ~ 0.1 – 2 keV show a localized enhancement at $L \sim 4.3$ – 4.5 . It is notable that the enhancement of these lower-energy electrons (~ 0.1 – 2 keV) to lower L-shell ($L \sim 4.3$ – 4.5) coincided with the arc detachment. In order to check the structure of electrons and ions near the inner edge of the plasma sheet for other orbits, we examined the LEP-e, MEP-e, and MEP-i E-t spectra for the previous and following orbit (supplementary Figure F1). Broadly, the electron fluxes for all the orbits show similar features near the inner edge of the electron plasma sheet; however, the localized enhancement of low-energy electrons (~ 0.1 – 2 keV) at $L \sim 4.3$ – 4.5

around the time of arc detachment (~ 1230 UT) was not observed for the previous and following orbit. In addition, E-t spectra for MEPe show a slight nose-like kink structure at 1230 UT, a common feature of convectively drifting electrons, not observed in the other orbits.

In MEPe E-t spectra (Figure 6c), the flux of particles towards lower L-shells appears to be energy dependent. The lower-energy component ($< \sim 20$ keV) was penetrated deeper to $L \sim 4.3$ at ~ 1230 UT in comparison to the higher-energy component ($> \sim 20$ keV), which shows an inward penetration to $L \sim 4.7$ at ~ 1300 UT. For electrons of energies < 1 keV, the energy of electrons decreases as they penetrated deeper towards lower L-shells (LEPe E-t spectra). This feature of decreasing electron energy at deeper L-shells can be also recognized in the MEPe E-t spectra (panel c) at energies < 10 keV at ~ 1220 – 1230 UT.

The MEPI E-t spectra (panel d) also show the presence of two components in the energy L-shell dispersion. The ions of energies > 20 keV show a multiple nose-like structure at ~ 1200 – 1215 UT. At 1200–1215 UT, a narrow depletion region is observed for ions of energy ~ 20 – 30 keV. The flux of ions of energies < 20 keV remains invariably higher in comparison to higher-energy (> 20 keV) ions at the entire L-shell.

Figure 7 shows the (a) electric field and (b) magnetic field variations in the SM coordinates, (c) electric and (d) magnetic field deviations from their 20-minute running averages, frequency-time wave diagrams obtained from PWE/OFA for (e) electric field, (f) magnetic field, and (g) DC-512 Hz electric field at 1200–1330 UT. The two solid black curves in panels (e) and (f) represent local cyclotron frequencies (f_{ce}) and $0.5f_{ce}$, respectively. The interval between two dashed lines indicates the presence of the arc. The cadence of electric field and magnetic field data is ~ 8 seconds, the spin period of the Arase satellite. The Arase measures two electric field components and the third component is estimated by assuming that the electric field component parallel to the ambient magnetic field is zero. The variations of very small magnitude (~ 1 – 2 mV/m) in all three components of the electric field are observed almost during the entire considered interval at 1200–1330 UT. In the magnetic field (Figure 7d), no recognizable variation is observed during the crossing of detached arc at ~ 1224 – 1251 UT, except for the two sets of small perturbations (± 1 nT) at ~ 1240 UT and ~ 1300 UT. Based on these observations, we infer that there are no recognizable field-aligned currents (FACs) associated with the detached auroral arc (e.g., Keiling et al., 2009).

The wave at ~ 1 kHz observed continuously during 1215–1325 UT in OFA-E and OFA-B is chorus emission (panels e and f). Since these waves are observed continuously during the interval 1215–1325 UT irrespective of the arc crossing by the satellite, we infer that the presence of these waves does not hold any particular relation with the detached arc. The multihundred Hz emission at 1230–1240 UT in panel (e) is an electrostatic hiss. The multihundred Hz emission at ~ 1243 – 1253 UT in panels (e) and (f) is an electromagnetic hiss. The 60–100 Hz signal at ~ 1235 – 1240 UT in panel (g) is an artificial noise. This noise was observed in OFA-E (panel e) and EFD (panel g), and also in the electric field (panels c and d).

3.4. Model Simulations

With an objective to explain the physical mechanism responsible for the penetration of lower-energy plasma to the lower radial distance around the time of arc detachment, we simulate electron and proton flux by using the BATS-R-US-CIMI model. Figure 8 shows the simulated proton flux (omnidirectional flux) as a function of time and radial distance (R [RE]) at five different energies (from ~ 1.7 to 17.7 keV) at a fixed MLT (01 MLT) where the arc detachment was observed. The dashed line in the figure highlights the approximate time of the arc detachment. Corresponding to the decreasing trend of IMF Bz from 1000 UT and ensuing southward turning at 1100 UT (Figure 2), the flux increases at all energies after ~ 1030 UT at $R \sim 7$ – 8 . The enhanced flux at higher R-values that moves towards lower R-values with the progression of time is known as the earthward penetration of plasma. Figure 8 shows two such earthward penetration events. During the first inward penetration event, the cloud of plasma moved from $R \sim 7$ at 1100 UT to $R \sim 4$ at 1230 UT. By contrast to this slow earthward motion, during the second inward penetration event, a cloud of plasma moved from $R \sim 7$ at 1215 UT to $R \sim 4$ at 1240 UT.

Figure 9 shows the simulated electron flux as a function of time and R [RE] at five different energies at a fixed MLT (01 MLT) where the arc detachment was observed. In similarity with proton flux, the enhancement in electron flux is initially observed at higher R-values ($R \sim 6.5$ – 7.5) for all energies after ~ 1030 UT onwards. This enhanced flux at higher R-values was penetrated inward in the earthward direction, and at 1200–1230 UT, the increased flux is observed at $R \sim 4$ for ~ 3 – 10 keV. At 1.7 keV, the inward motion of flux to $R < 5$ is not successfully simulated; however, a tendency of inward motion from $R \sim 7$ to $R \sim 5$ is observed at 1100–1130 UT. At 17.7

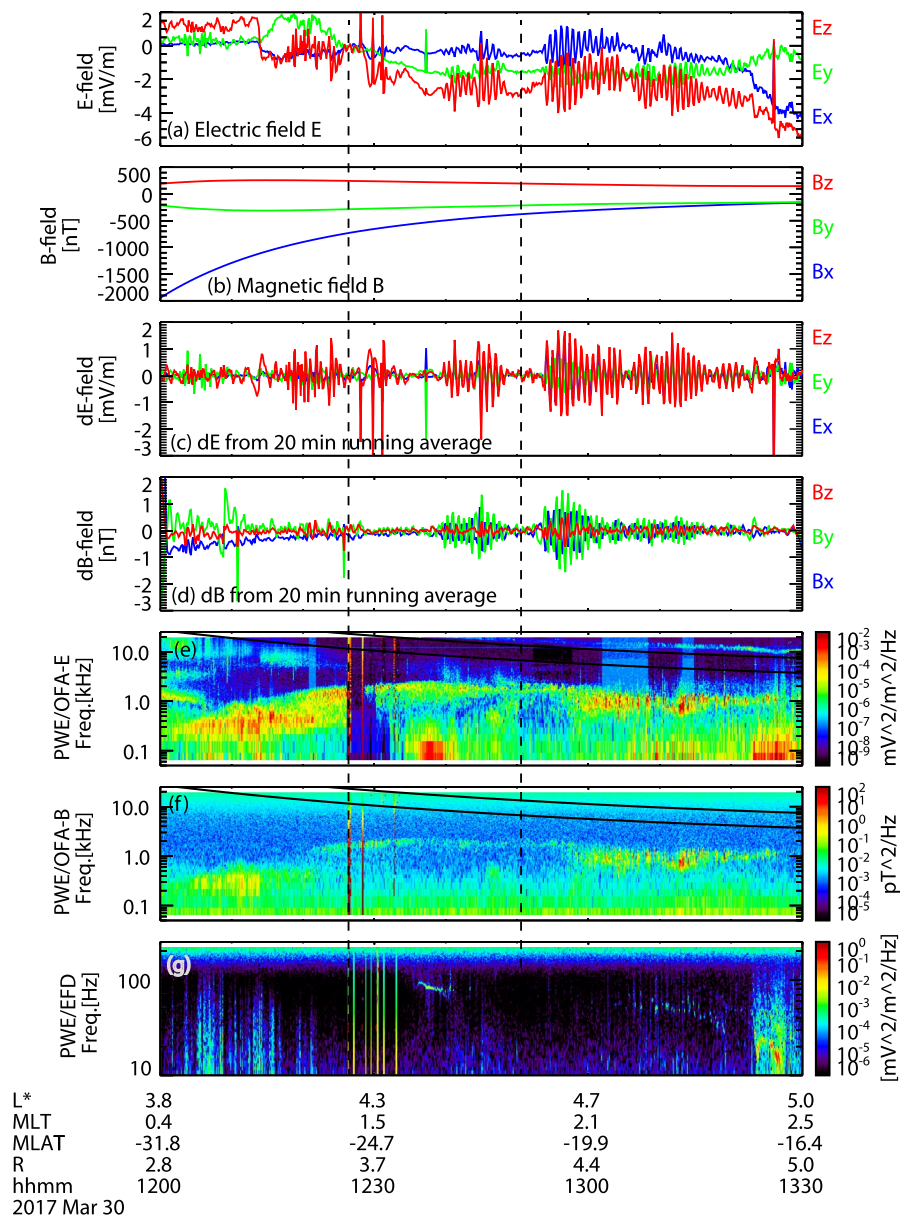


Figure 7. (a) Electric field and (b) magnetic field variations in GSM coordinates, (c) electric and (d) magnetic field deviations from their 20-minute running average values, frequency-time diagrams obtained from PWE/OFA for (e) electric field, (f) magnetic field, and (g) DC-512 Hz electric field at 1200–1330 UT. Solid black lines in panels (e) and (f) represent local cyclotron frequency (f_{ce}) and $0.5f_{ce}$.

keV, the inward motion of flux below $R < 5$ is not discernible because of the enhanced flux during the entire considered period. The second penetration event is observed for ~ 3 – 10 keV with a tendency of inward motion at ~ 1215 – 1240 UT. The increased flux at $R \sim 4$ at 17.7 keV at 1200–1300 might be associated with the two aforementioned inward moving flux events.

In order to examine the variation of particle flux with a radial distance, we plot proton and electron fluxes at 0100 MLT as a function of energy and R [RE] (energy spectra) in Figures 10 and 11, respectively, at different times 1100–1300 UT in panels a–e. For both ions and electrons, the time-sequential energy spectrum plots show the presence of inward moving flux. Initially, at 1100 UT, enhanced flux is observed at $R \sim 5.5$ – 7.5 for the protons of energy ~ 20 – 200 keV. As time progresses, the flux moves inward, and at 1200 UT, the increased flux is observed at $R \sim 4$ – 6 for protons of energy ~ 20 – 80 keV. At 1230–1240 UT, the increased flux moved further inward

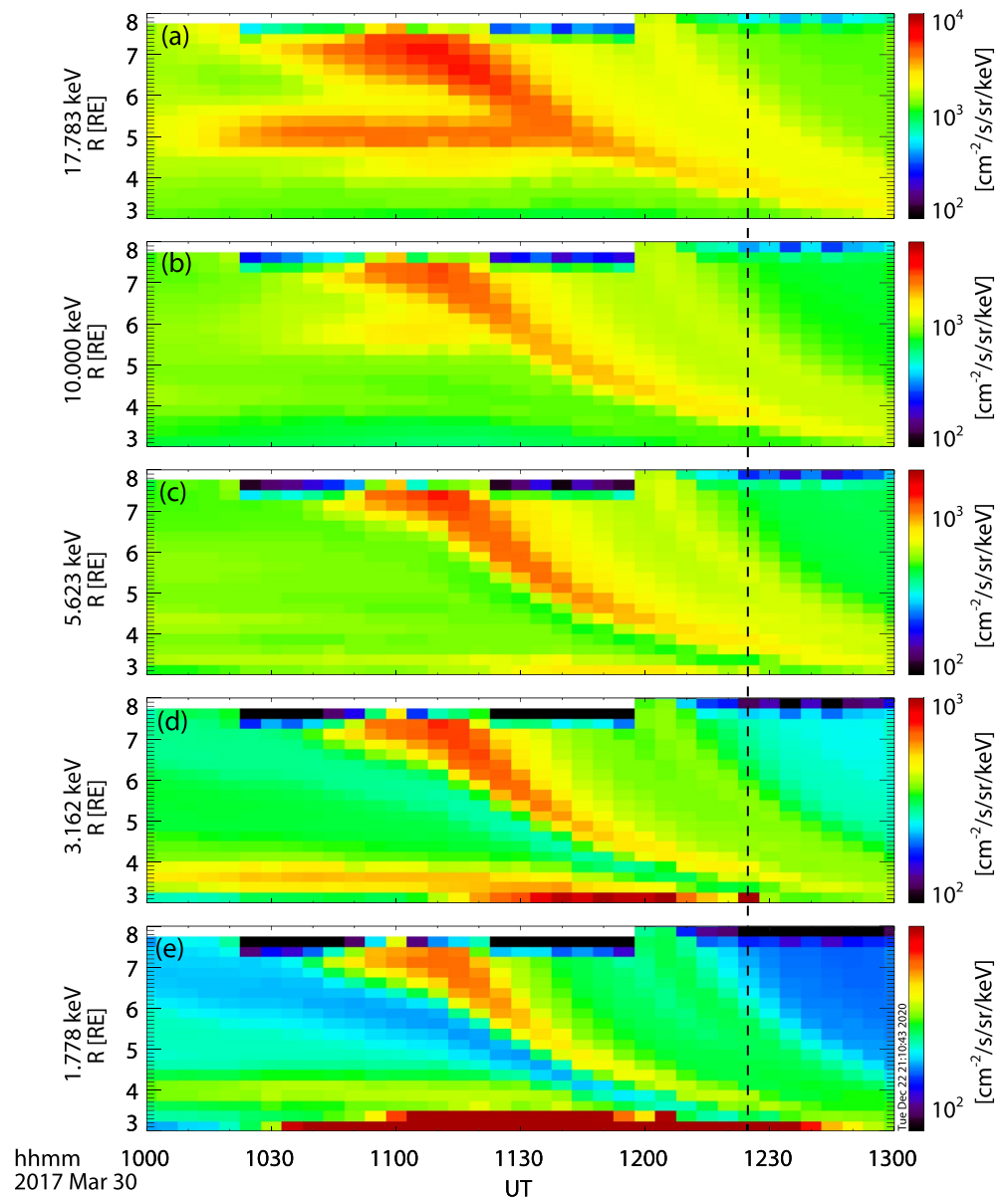


Figure 8. Simulated proton flux as a function of time and radial distance (R [RE]) at five different energies (from ~ 1.7 to 17.7 keV). The dashed line highlights the approximate time of arc detachment.

to $R \sim 3.5$ – 5 for protons of energy ~ 20 – 80 keV. The proton flux below 20 keV does not show any considerable change at different times, similar to the Arase observations.

Unlike proton flux, considerable change is observed for electron flux of energy ~ 8 – 80 keV at different times. At 1100 – 1130 UT, the lower R -values ($R < 4$) seem to be completely devoid of electron flux of energy < 10 keV. For electrons of energy ~ 8 – 80 keV, the flux enhancement is initially observed at $R \sim 4.5$ – 6.5 at 1130 UT. With the progression of time, the electron flux shows the feature of inward motion towards the lower R -values. At 1230 – 1300 UT (around the time of arc detachment), the enhanced flux moves inward to $R \sim 3.5$ – 4.5 for electrons of energy ~ 8 – 40 keV. The electron flux of energy < 10 keV is also enhanced at $R < 4$ at 1230 – 1300 UT; however, no change is observed for electrons of energies < 5 keV for all R -values. Thus, although simulations successfully show the earthward motion of lower-energy electrons (~ 8 – 40 keV), it could not reproduce the electron flux (< 2 keV) responsible for the arc detachment.

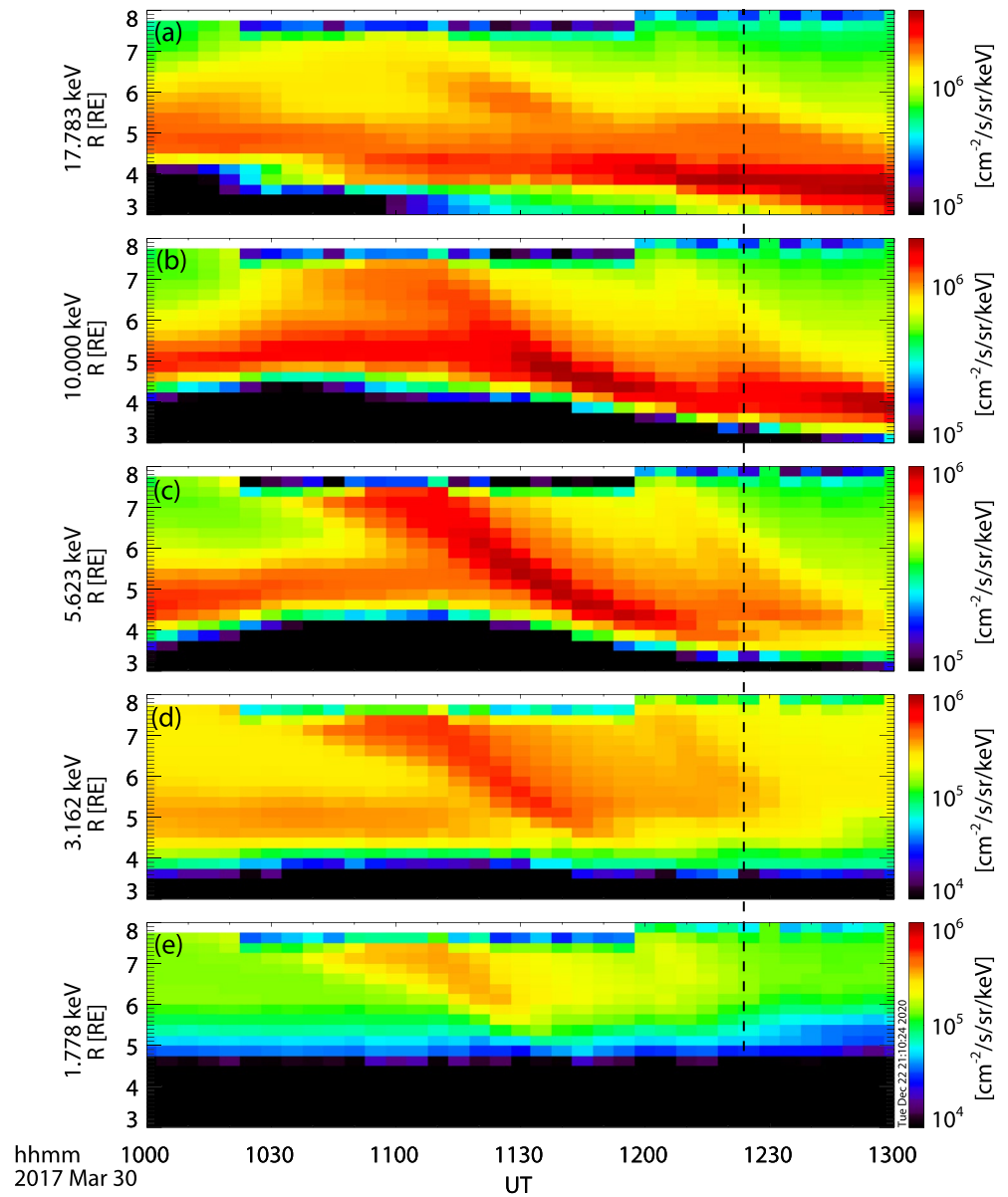


Figure 9. Same as Figure 8 but for electron flux.

3.5. Estimated Auroral Intensity Based on LEPe Flux

One of the notable findings from the conjugate measurements of the Arase satellite and ground-based ASI is that the penetration of lower-energy electrons ($\sim 0.1\text{--}2$ keV) to lower L-shell (LEPe E-t spectra) coincided with the arc detachment. Therefore, in order to examine the relationship between low-energy electrons and equatorward arc detachment, we estimated the intensity of the 630.0-nm and 557.7-nm emissions by using the electron flux data obtained by LEPe. The LEPe onboard the Arase measured the three-dimensional distribution function of electrons with energies of ~ 19 eV–19 keV in the magnetosphere. It is known that electrons in the loss-cone ($\sim 2^\circ$ at the equator $L\sim 6$) can precipitate in the ionosphere. Thus, in order to estimate the emission intensity caused by the precipitation of energetic charged particles, the most realistic approach would be to use the field-aligned flux. The level-3 data of LEPe provide the pitch angle distribution of electron flux with a bin size of 11.25° . Unfortunately, the angular coverage and resolution of the instrument were not suitable for exclusively measuring the field-aligned flux (0° and 180°) at 1100–1300 UT. Therefore, we have used the level-2 data of electron flux for pitch angles ($0^\circ\text{--}15^\circ$) close to the loss cone angle to calculate the emission intensity. Note that the use of fluxes

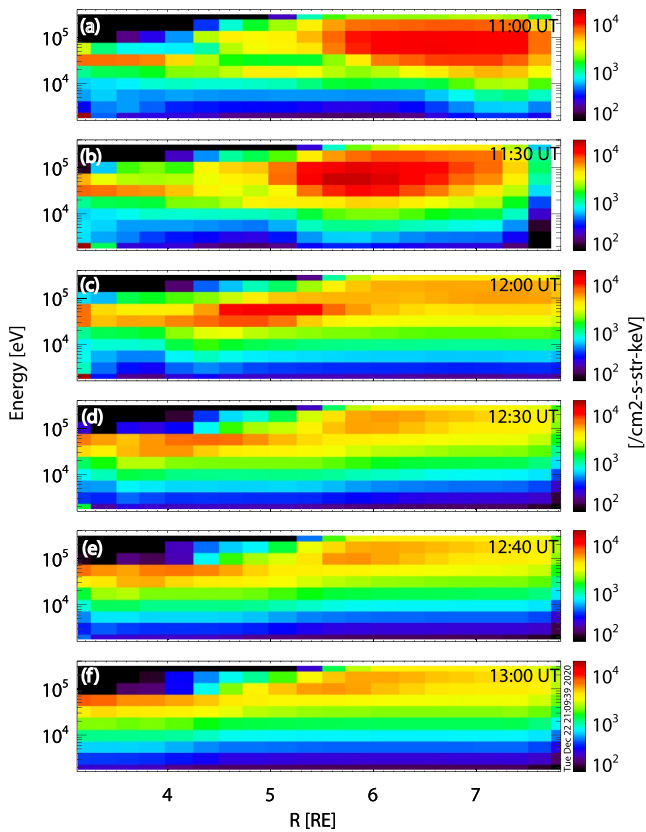


Figure 10. Simulated proton flux as a function of energy and R [RE] (energy spectra) at 0100 MLT.

slightly off the loss cone might cause uncertainty in estimating the emission intensity. Further, in order to avoid the influence of the satellite potential, we have used electron flux ≥ 100 eV.

It is established that keV electrons generate the green-line emissions with a maximum emission rate at ~ 10 keV, whereas the emission rate for red-line emissions (630.0 nm) maximized at ~ 0.5 keV (Banks et al., 1974). It was shown that the $O^1(D)$ state is mainly produced by the direct electron impact of low-energy electrons < 300 eV (Shepherd et al., 1980; Solomon et al., 1988). For $O^1(S)$, the energy transfer from $N_2(A^3\Sigma_u^+)$ is considered as the main source when high-energy electrons precipitate into the atmosphere, whereas the direct electron impact excitation of atomic oxygen becomes the main source for lower-energy electron precipitation (e.g., Torr & Torr, 1982; Shiokawa & Fukunishi 1990). Shiokawa and Fukunishi (1990) calculated the column emission rates for auroral 630.0-nm emission (4.28 photons $\text{cm}^{-2} \text{s}^{-1}$ for 0.5-keV electrons and 1.85 photons $\text{cm}^{-2} \text{s}^{-1}$ for 5-keV electrons) and 557.7-nm emission (1.3 photons $\text{cm}^{-2} \text{s}^{-1}$ for 0.5-keV electrons and 15 photons $\text{cm}^{-2} \text{s}^{-1}$ for 5-keV electrons) for precipitating electrons of energies 0.5 keV and 5.0 keV. We have interpolated/extrapolated these column emission rates to cover the entire spectrum of energies 0.1–19 keV measured by the LEPe (column emission rate of 4.28/1.3 photons $\text{cm}^{-2} \text{s}^{-1}$ for electrons of energies < 2 keV and 1.85/15.0 photons $\text{cm}^{-2} \text{s}^{-1}$ for electrons of energies > 2 keV). Although this method is a very rough estimation, it may give an approximation of the auroral intensities produced by precipitating electrons in the ionosphere.

Figure 12 shows the observed (at three different mapping altitudes of 200, 300, and 400 km for the red line and 100, 120, and 150 km for the green line; similar to panels (e) and (f) of Figure 6) and calculated intensities of the 630.0-nm and 557.7-nm emissions at the ionospheric footprint of the Arase satellite on a linear scale, plotted versus universal time (UT). The location of the Arase satellite with respect to L-value, MLT, MLAT, and radial distance

(R) is also shown at the bottom of the figure. The data gap in estimated intensities is caused by the data gap in the LEPe particle flux associated with the change in observation mode, also seen in the LEPe energy time spectra in Figure 6. The estimated auroral intensity at 630.0 nm began to increase after ~ 1220 UT, showing a peak at ~ 1235 – 1240 UT, and gradually decreased thereafter. The peak of the calculated auroral intensity at 630.0 nm coincided with the peak of observed emission intensity at 300 km (indicated by a dashed red line). At 557.7 nm, the calculated auroral emission intensity began to increase after 1230 UT and peaks at ~ 1240 – 1245 UT, coinciding with the peak in the observed intensity at 120 km (indicated by a dashed green line). These results suggest that the height of emission might be 120 km and 300 km for the green and red lines, respectively. While the observed auroral intensity shows an enhancement of ~ 1700 Ry over the background, the estimated auroral intensity shows an increase of roughly ~ 550 Ry for the red line. The magnitude of the estimated 557.7-nm intensity (~ 2000 Ry) was much smaller than the observed intensity (5500 Ry). By using the above magnitudes of the peak emission intensity, the ratio between the red and green lines comes out to be ~ 3.2 and ~ 3.6 for observed and estimated auroral intensity, respectively. Thus, although the magnitude of observed and calculated emission intensities at both 557.7-nm and 630.0-nm emission is considerably different, their ratio remains reasonably close. It is notable that the peak latitude of observed and calculated auroral intensities matches considerably well for both 630.0-nm and 557.7-nm emissions. These observations indicate that the localized enhancement of low-energy (~ 0.1 – 2 keV) electrons at the inner edge of the electron plasma sheet observed by LEP-e might be the source of the detached auroral arc observed at Gakona.

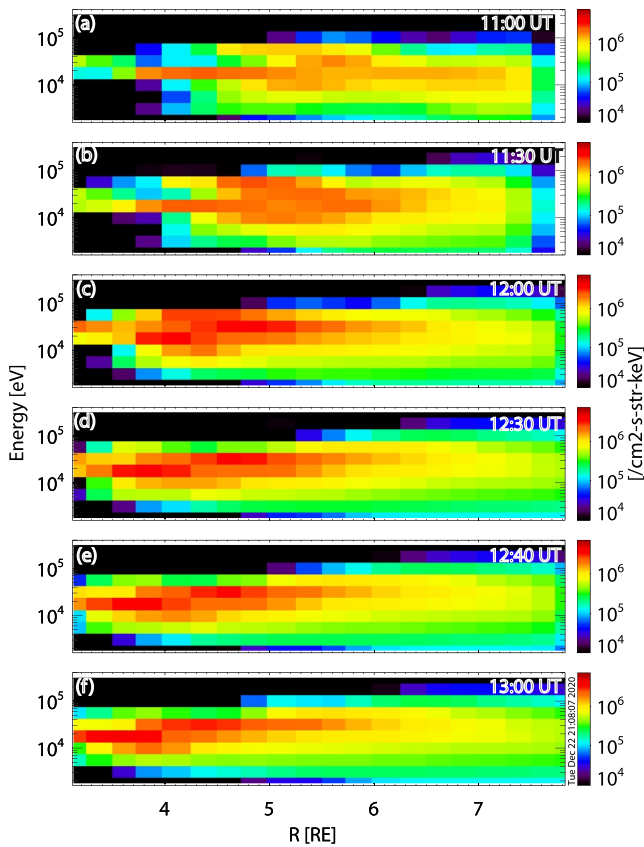


Figure 11. Same as Figure 10 but for electron flux.

4. Discussion

Recent studies have reported the common feature of the equatorward detachment of the auroral arc from the main auroral oval, e.g., SAR arc (Shiokawa et al., 2009a, 2017; Takagi et al., 2018; Inaba et al., 2020) and STEVE (Gallardo-Lacourt et al., 2018; Yadav et al., 2021). These studies raise the fundamental questions that what causes the equatorward detachment of arc from the main oval and how it is linked to the inner magnetosphere. There is no study carried out so far shedding light on this particular aspect. In this study, we present conjugate measurements from an all-sky imager and the Arase satellite for an auroral arc event that occurred on 30 March 2017 at ~1230–1300 UT (~0130–0200 MLT). Although conjugate measurements of satellites crossing the arc have been reported by earlier studies (Inaba et al., 2020; Shiokawa et al., 2020 and reference therein), the present observations are unprecedented because the ionospheric footprints of the Arase satellite crossed the auroral arc at the time of its detachment from the main auroral oval. In order to investigate the detachment mechanism, we also use model simulations from the BATS-R-US-CIMI. The equatorward detachment of this arc from the main auroral oval appeared similar to the SAR arc and STEVE. We also checked the anisotropy of the low-energy electrons by the pitch angle distribution of LEPe particle flux (not shown here). The enhancement of particle flux around the time of arc detachment is found to be isotropic. It is notable that the observed auroral arc is spectrally different from SAR arc (subvisual red-arc) and STEVE (visible purple arc) because it consists of emissions in both the red and green lines. The in-situ measurements from the Arase satellite indicate that this arc occurred at the base of the flux tube that is outside the plasmopause. By contrast, SAR arcs and STEVE are reported to occur at or just inside the plasmopause (Cornwall et al., 1971; Kozyra et al., 1997; Chu et al., 2019).

Although the detachment of the auroral arc from the main auroral oval is observed at ~1225 UT, the movement of the auroral oval in the equatorward direction began from 1130 UT. The process of arc detachment occurred during the recovery phase of the substorm activity. After detachment, the arc also shifts in the equatorward direction. The equatorward motion of the auroral oval corresponds to the inward motion of source plasma in the inner magnetosphere. The coordinated satellite measurements at $L \sim 3.8$ – 5.0 during 1200–1330 UT show the enhancement of low-energy electrons (~ 0.1 – 2 keV) at the inner boundary of the electron plasma sheet at $L \sim 4.3$ – 4.5 (Figure 6). The MEP-e electron flux shows the presence of a nose-like kink structure around the time of detachment (~ 1230 UT), plausibly indicating a fresh particle penetration into the inner magnetosphere. The simulation from BATS-R-US-CIMI shows two events of earthward motion of plasma from $R \sim 7$ to $R \sim 4$ at 1100–1230 UT and 1215–1240 UT. Although the model could not reproduce the lower-energy component responsible for the arc detachment (~ 0.1 – 2 keV), it successfully simulated the enhancement of low-energy electron flux (~ 8 – 40 keV) at the lower radial distance ($R \leq 4$) around the time of arc detachment (1230–1240 UT) (Figure 11). These observations indicate the connection of arc detachment with the enhancement of low-energy electrons at the inner boundary of the electron plasma sheet. This hypothesis is further supported by estimating the emission intensities for both 630.0 nm and 557.7 nm based on the LEPe flux data. The peak latitude and time of the calculated auroral emission intensity coincided with that of the observed intensities for both 630.0 nm and 557.7 nm (Figure 12).

The difference in magnitude between the observed and estimated emission intensity may be primarily caused by the assumptions in deriving the column emission rates (Shiokawa & Fukunishi, 1990), unavailability of field-aligned flux in the loss cone, and interpolation/extrapolation of the two-column emission rates (0.5 keV and 5 keV) to cover the entire energy spectrum of LEPe (~ 0.1 – 19 keV). In addition, the sensitivity of the LEPe electrostatic detector in measuring the absolute flux might also partially account for the difference in magnitude of the observed and estimated emission intensity. Even though Shiokawa and Fukunishi (1990) took into account all the important processes responsible for the excitation of atomic oxygen to $O^1(D)$ and $O^1(S)$, some other processes

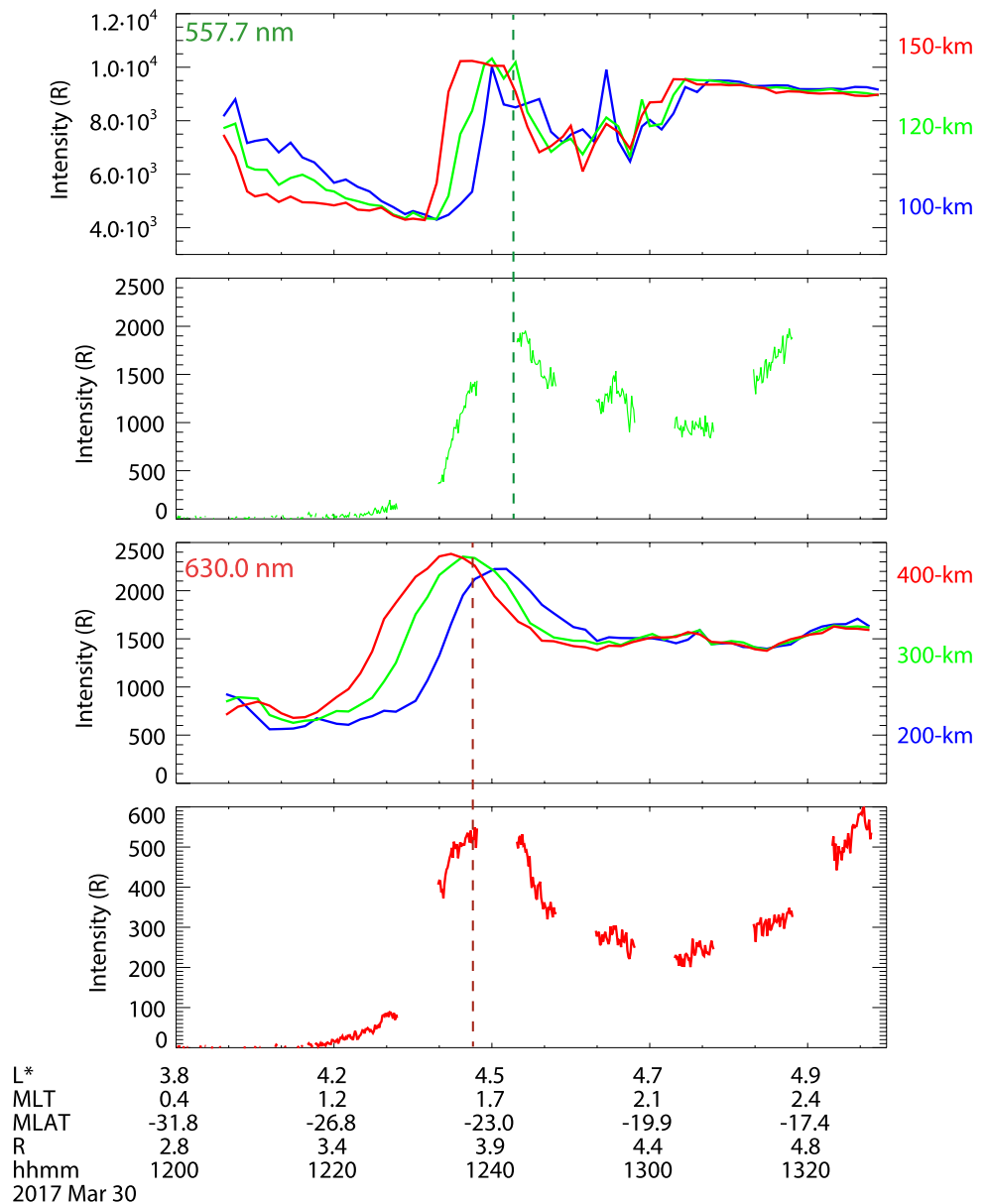


Figure 12. Observed (at three different altitudes) and estimated intensities for 557.7-nm (upper two panels) and 630.0-nm (lower two panels) emission lines at the ionospheric footprint of the Arase satellite during the interval 1200-1330 UT.

might be missing, e.g., the energy transfer from $N_2(A^3\Sigma_u^+)$, which is considered as the main source for $O(^1S)$ when high-energy electrons precipitate into the atmosphere. However, it is noteworthy that, in spite of such rough approximation, a good correspondence exists between the peak latitude of the observed and calculated auroral intensity for both the red and green lines. These calculations suggest that the detached equatorward moving auroral arc might hold association with the localized enhancement of low-energy electrons at lower L-shells.

Anger et al. (1978) reported the arc-like auroral emissions in the northern hemisphere equatorward of the auroral particle precipitation region and they termed these arcs as "detached arcs." Observed by Isis 2 satellite scanning photometer, these "detached arcs" did not show any enhancement in the 630.0-nm emission. By contrast, we observe detached arc in both the red and green lines. Later, Wallis et al. (1979), by using the energetic particle detector onboard Isis 2, revealed that these "detached arcs" occurred at the feet of the field lines having a trapped population of 1-10 keV electrons as well as the usual higher-energy radiation belt particles. Above these detached arcs, they observed the precipitation of these trapped particles at all energies up to 210 keV. Thus, our

observations further support the hypothesis put forth by Wallis et al. (1979) that trapped residual plasma sheet fluxes might provide the source populations for the detached arc.

The energy-time spectrum observed by the Arase satellite reveals that for both ions and electrons, energy time dispersion has two components that depend on energy: <20 keV and >20 keV, referred to as lower- and higher-energy components, respectively. While the low-energy electrons (<10 keV) was penetrated down to $L\sim 4.1$, the higher-energy electrons (>20 keV) show a maximum penetration at $L\sim 4.7$. By contrast, both low- and high-energy ions were penetrated to $L\sim 3.8$, although the flux of lower-energy (<20 keV) ions is found to be much higher ($\sim 10^6$) compared to higher-energy (>20 keV) ions ($\sim 10^5$). This indicates that ions at all energies were penetrated deeper towards lower L-shells in comparison to electrons. By using simulations, Ejiri et al. (1980) showed that electrons cannot penetrate inside the plasmopause, whereas given sufficient time ions can penetrate inside the plasmopause at every MLT but do more readily in the dusk-to-midnight region. This probably explains the penetration of ions deeper in the inner magnetosphere compared to electrons as the present event corresponds to the midnight sector (~ 00 – 02 MLT).

The ion E-t spectra in Figure 6d also show the presence of a narrow depletion region at ~ 20 – 30 keV at 1200–1215 UT. A sharp and deep dip of ions at around 10 keV in the ion spectra was first reported by Shirai et al. (1997) by using the Akebono satellite. In order to explain this drop-off of ions, they proposed that the lower-energy boundary of the drop-off demarcates the open/closed character of the drift orbits, only below which continuous supply from the magnetotail is present. The simulations by Ejiri et al. (1980) also showed that there is a characteristic distinguished energy (15–25 keV) at which protons penetrate to the lower L-shells than particles with lower or higher energies. For ions, a nose-like structure is observed at $L\sim 3.8$ – 4.2 for >20 -keV energy component. Nose-structures, which are common features of convectively drifting particles and indicate the fresh transport of plasma into the inner magnetosphere, have been reported extensively in the energy-time spectrograms of the in-situ measured ion fluxes by various magnetospheric missions (e.g., Smith & Hoffman, 1974; Vallat et al., 2007; Dandouras et al., 2009; Ferradas et al., 2016; Ferradas et al., 2018). The concurrent ion and electron E-t spectra provide information about the relative location of the ion plasma sheet with respect to the localized enhancement of low-energy electrons. The observations suggest that the enhanced low-energy electrons (~ 1220 – 1300 UT) and the associated equatorward moving detached arc is located inside the ion plasma sheet.

Comparison of electron structures for the concerned orbit with the previous and following orbit (Figure F1 in Supporting Information S1) revealed that the peculiar feature is observed around the time of arc detachment (~ 1230 UT) in terms of the localized enhancement of low-energy electrons (~ 0.1 – 2 keV) at $L\sim 4.3$ – 4.5 , not observed for the other orbits. In addition, E-t spectra for MEP-e show a slight nose-like kink structure at ~ 1230 UT (Figure 6c), which is also not observed for the other orbits. This probably indicates the penetration of fresh particles in the inner magnetosphere around the time of arc detachment. Previous studies suggested that the combined action of global convection and substorm-associated dipolarization and electric field variations inject plasma deeper towards the Earth (Fok et al., 1999; Ganushkina & Pulkkinen, 2002). While explaining the formation of intense nose structures, Ganushkina et al. (2000, 2001) suggested that such nose structures can occur under the concurrent action of short-lived impulsive electric fields and convection electric fields. It was found out that during a substorm ion population may move from geostationary orbit into the plasmasphere up to $L\sim 4.7$ in ~ 1 hour (Ganushkina et al., 2001), whereas large-scale convection leads to the nose structure formation in >5 hours (Buzulukova et al., 2003).

In the present case, two small substorm type activities are observed in the AU/AL indices at 1130–1225 UT and 1235–1310 UT. We checked the GOES satellite particle flux data (not shown here), but could not find the signature of dipolarization and substorm-associated injection event at the geostationary orbit. Turner et al. (2015) proposed that the interaction of electrons with a fast magnetosonic wave in the Pi2 frequency range inside the plasmasphere may cause the injection of electrons with energy ≤ 250 keV to $L \leq 4$. Note that the study of Turner et al. (2015) was based on 47 injection events and all events occurred shortly after dipolarization signatures. For the present case, at the magnetospheric footprint of the detached arc (Arase observations), no considerable variation in electric and magnetic fields is observed (Figure 7a–d), indicating the absence of a fast magnetosonic wave in the Pi2 frequency range in the deep injection region. In addition, the magnetic field observed by Arase showed no signature of dipolarization at the magnetospheric footprint of the detached arc. Thus, although the AL-index depicts two-substorm-like activities at $\sim 11:30$ and $\sim 12:40$ UT, the Arase and GOES observations do not show

any clear signature of substorm-associated dipolarization and transient electric field at least at the site of measurement. However, the possibility of a transient electric field outside of the measurement site cannot be discarded.

The BATS-R-US–CIMI simulations show the signatures of enhanced localized electric fields around the geosynchronous orbit as the increased values of the dawn-to-dusk electric field is observed around the geosynchronous orbit particularly in the midnight-to-dawn sector that is around the time of Arase observations. These enhanced localized electric fields inside the geosynchronous orbit might be sufficient to accelerate particles towards the lower L-shell. The BATS-R-US–CIMI successfully reproduced two inward penetration events around the time of detachment, probably demonstrating the enhanced convection. During the first penetration event, the cloud of plasma moved from $R \sim 7$ at 1100 to $R \sim 4$ at 1230 UT. In contrast to this slow earthward motion, during the second penetration event, plasma moved from $R \sim 7$ at 1215 UT to $R \sim 4$ at 1240 UT. The BATS-R-US–CIMI model successfully simulated the build-up of lower-energy electrons (~ 8 – 40 keV) at the lower radial distance $R \leq \sim 4$ around the time of arc detachment. However, the enhanced localized electric fields could not reproduce the lower-energy component responsible for the arc detachment (< 2 keV), because no change in the electrons of energy < 5 keV is observed in the simulations. Thus, although the model successfully reproduced the convection features qualitatively, it could not reproduce the energy component responsible for the arc detachment.

The simulations also reproduced the enhanced convection features, e.g., the energy L-shell dispersion, i.e., inward penetration of lower-energy electrons to the lower L-shell, in similarity with the Arase observations. The reproducibility of these features by global simulation is important to understand the generation of equatorward auroral motion. The simulated AL index, although did not show two-substorm-like activities, it showed negative values from ~ 1130 onwards, in similarity with the observed AL index but with a much lesser magnitude (see Figure F2 Supporting Information S1). Since the simulation cannot reproduce the reconnection precisely, the simulated AL index (and other parameters associated with reconnection) might be underestimated as compared to the observations. However, as explained above, the simulation successfully captures the inward convection of particle flux even when the simulated AL-index underestimates the observed AL-index. These weak variations might represent enhanced magnetospheric convection in the simulations. Since the observations also did not show any signatures of substorm-associated dipolarization, we speculate that the convection enhancement might play a role in creating such a localized enhancement of low-energy electrons at the inner edge of the electron plasma sheet.

5. Conclusion

This study presents unique observations of an equatorward detachment of the auroral arc from the main oval (using an ASI at Gakona) and magnetically conjugate measurements made by the Arase satellite in the inner magnetosphere on 30 March 2017. The arc detachment is observed in both red and green lines in the recovery phase of a substorm. Results reveal that the equatorward detachment of arc coincided with the localized enhancement of low-energy electrons (~ 0.1 – 2 keV) at the inner boundary of the electron plasma sheet and that the mechanism that creates the arc detachment is occurring inside the ion plasma sheet. In order to examine the association of these enhanced low-energy electrons with the equatorward detached arc, we estimated the auroral intensity for both 630.0 nm and 557.7 nm by using the low-energy electrons (0.1 keV–19 keV) flux data. In spite of the rough estimation, the peak of the observed and calculated auroral intensity for both 630.0 nm and 557.7 nm shows reasonably good correspondence. These results indicate the linkage between the detached arc and the inner magnetosphere via the localized enhancement of low-energy electrons (~ 0.1 – 2 keV) at the inner edge of the electron plasma sheet. In order to understand the conditions in the inner magnetosphere around the time of arc detachment, we used the BATS-R-US–CIMI model. Although the simulation could not reproduce the lower-energy component (< 2 keV) responsible for the arc detachment, it successfully reproduced two earthward convection events and buildup of lower-energy electrons (~ 8 – 40 keV) at the lower radial distance $R \leq \sim 4$ around the time of arc detachment. Simulations also successfully reproduced the features of steady-state convection in similarity with the Arase observations.

Data Availability Statement

The optical data obtained at Gakona are available through ISEE/Nagoya University. Quick-look plots of the OMTI data are available at <http://stdb2.isee.nagoya-u.ac.jp/omti/> and the data can be accessed from the ERG Science Center operated by ISAS/JAXA and ISEE/Nagoya University (<https://ergsc.isee.nagoya-u.ac.jp/data/ergsc/>)

ground/camera/omti/asi/). The data from the ERG (Arase) satellite were obtained from the ERG Science Center (ERG-SC) operated by ISAS/JAXA and ISEE/Nagoya University (https://ergsc.isee.nagoya-u.ac.jp/data_info/index.shtml.en; Miyoshi et al., 2018b). The present study analyzed LEP-e-L2 v02_02 (10.34515/DATA.ERG-04002) (Wang et al., 2018), MEP-e-L2 v01_02 (10.34515/DATA.ERG-02001) (Kasahara et al., 2018c), MEP-i-L2 v02_00 (10.34515/DATA.ERG-03001) (Yokota et al., 2018), PWE/EFD/E_spin-L2 v04_01 (10.34515/DATA.ERG-07000) (Kasahara et al., 2018d), PWE/HFA-L2 v01_02 (Kasahara et al., 2018e), PWE/OFA-L2 v02_01 (10.34515/DATA.ERG-08000) (Kasahara et al., 2018f) and MGF-L2 v04.04 (10.34515/DATA.ERG-06001) (Matsuoka et al., 2018b), and L2 v03 orbit (10.34515/DATA.ERG-12000) (Miyoshi et al., 2018c) data. Simulation results have been provided by the Community Coordinated Modeling Center at Goddard Space Flight Center through their public Runs on Request system (<https://ccmc.gsfc.nasa.gov>; run number: Naoko_Takahashi_082420_1). The solar wind input used in the simulations is taken from the DSCOVR L2 data https://omniweb.gsfc.nasa.gov/ftpbrowser/dscovr_merged.html. The solar wind parameters and AU/AL index were obtained from SPDF, NASA, USA (https://omniweb.gsfc.nasa.gov/form/omni_min_def.html). The solar wind parameters and W-parameters for driving the Tsyganenko-Sitnov (TS05) model were provided by the TS05 web repository (http://geo.phys.spbu.ru/~tsyganenko/TS05_data_and_stuff/). The all-sky imager at Gakona was calibrated using optical facilities of the National Institute of Polar Research, Japan (Ogawa et al., 2020). THEMIS ASI data can be viewed via the University of Calgary data portal located online (<http://data-portal.phys.ucalgary.ca/>). GOES data are archived at NOAA's National Centers for Environmental Information (NCEI) <http://satdat.ngdc.noaa.gov/sem/goes/data/full/>.

Acknowledgments

We appreciate Yuka Yamamoto and Takumi Adachi of Nagoya University for their skillful support for continuous operation of the all-sky camera at Gakona. This work is supported by JSPS KAKENHI (16H06286, 15H05747, 17H00728, 20H01959, 21H04518, 21KK0059), and JSPS Bilateral Joint Research Projects (JPJSBP120194814, JPJSBP120192504).

References

- Anger, C., Moshupi, M., Wallis, D., Murphree, J., Brace, L., & Shepherd, G. (1978). Detached auroral arcs in the trough region. *Journal of Geophysical Research*, 83, 2683. <https://doi.org/10.1029/ja083ia06p02683>
- Angelopoulos, V., Cruce, P., Drozdov, A., Grimes, E. W., Hatzigeorgiu, N., King, D. A., et al. (2019). The Space Physics Environment Data Analysis System (SPEDAS). *Space Science Review*, 215. <https://doi.org/10.1007/s11214-018-0576-4>
- Banks, P. M., Chappell, C. R., & Nagy, A. F. (1974). A new model for the interaction of auroral electrons with the atmosphere: Spectral degradation, backscatter, optical emission, and ionization. *Journal of Geophysical Research*, 79(10), 1459–1470. <https://doi.org/10.1029/JA079i010p01459>
- Blanchard, G., Lyons, L., & Samson, J. (1997). Accuracy of using 6300 Å auroral emission to identify the magnetic separatrix on the nightside of Earth. *Journal of Geophysical Research*, 102(A5), 9697–9703. <https://doi.org/10.1029/96JA04000>
- Buzulukova, N. Y., Kovrazhkin, R. A., Glazunov, A. L., Sauvaud, J.-A., Ganushkina, N. Y., & Pulkkinen, T. I. (2003). Stationary nose structures of protons in the inner magnetosphere: Observations by the ION instrument onboard the Interball-2 satellite and modeling. *Cosmic Research*, 41, 3–12. <https://doi.org/10.1023/a:1022343327565>
- Chu, X., Malaspina, D., Gallardo-Lacourt, B., Liang, J., Andersson, L., Ma, Q., et al. (2019). Identifying STEVE's Magnetospheric Driver Using Conjugate Observations in the Magnetosphere and on the Ground. *Geophysical Research Letters*, 46, 12665, 12674. <https://doi.org/10.1029/2019GL082789>
- Cornwall, J. M., Coroniti, F. V., & Thorne, R. M. (1971). Unified theory of SAR arc formation at the plasmapause. *Journal of Geophysical Research*, 76, 4428–4445. <https://doi.org/10.1029/JA076i019p04428>
- Cole, K. (1965). Stable auroral red arcs, sinks for energy of Dst main phase. *Journal of Geophysical Research*, 70, 1689–1706. <https://doi.org/10.1029/JZ070i007p01689>
- Dandouras, I., Cao, J., & Vallat, C. (2009). Energetic ion dynamics of the inner magnetosphere revealed in coordinated Cluster-Double Star observations. *Journal of Geophysical Research*, 114, a, n, A01S90. <https://doi.org/10.1029/2007JA012757>
- Frey, H. U. (2007). Localized aurora beyond the auroral oval. *Reviews of Geophysics*, 45(1), 1003. <https://doi.org/10.1029/2005RG000174>
- Ejiri, M., Hoffman, R. A., & Smith, P. H. (1980). Energetic particle penetrations into the inner magnetosphere. *Journal of Geophysical Research*, 85, 653. <https://doi.org/10.1029/ja085ia02p00653>
- Ferradas, C. P., Zhang, J.-C., Spence, H. E., Kistler, L. M., Larsen, B. A., Reeves, G., et al. (2016). Ion nose spectral structures observed by the Van Allen Probes. *Journal of Geophysical Research-Space Physics*, 121, 12,025–12. <https://doi.org/10.1002/2016JA022942>
- Ferradas, C. P., Zhang, J.-C., Spence, H. E., Kistler, L. M., Larsen, B. A., Reeves, G. D., et al. (2018). Temporal evolution of ion spectral structures during a geomagnetic storm: Observations and modeling. *Journal of Geophysical Research-Space Physics*, 123, 179–196. <https://doi.org/10.1002/2017JA024702>
- Fok, M.-C., Buzulukova, N. Y., Chen, S.-H., Glocer, A., Nagai, T., Valek, P., & Perez, J. D. (2014). The Comprehensive Inner Magnetosphere-Ionosphere Model. *Journal of Geophysical Research: Space Physics*, 119, 7522–7540. <https://doi.org/10.1002/2014JA020239>
- Fok, M.-C., Moore, T. E., & Delcourt, D. C. (1999). Modeling of inner plasma sheet and ring current during substorms. *Journal of Geophysical Research-Space Physics*, 104, 14 557–14 569. <https://doi.org/10.1029/1999ja900014>
- Ganushkina, N. Y., & Pulkkinen, T. I. (2002). Particle tracing in the inner Earth's magnetosphere and the formation of the ring current during storm times. *Advances in Space Research*, 30, 1817–1820. [https://doi.org/10.1016/s0273-1177\(02\)00455-6](https://doi.org/10.1016/s0273-1177(02)00455-6)
- Ganushkina, N. Y., Pulkkinen, T. I., Sergeev, V. A., Kubyshkina, M. V., Baker, D. N., Turner, N. E., et al. (2000). Entry of plasma sheet particles into the inner magnetosphere as observed by Polar/CAMMICE. *Journal of Geophysical Research-Space Physics*, 105, 25 205–25 219. <https://doi.org/10.1029/2000ja900062>
- Ganushkina, N. Y., Pulkkinen, T. I., Bashkurov, V. F., Baker, D. N., & Li, X. (2001). Formation of intense nose structures. *Geophysical Research Letter*, 28, 491–494. <https://doi.org/10.1029/2000gl011955>
- Gallardo-Lacourt, B., Nishimura, Y., Donovan, E., Gillies, D. M., Perry, G. W., Archer, W. E., et al. (2018). A statistical analysis of STEVE. *Journal of Geophysical Research-Space Physics*, 123, 9893–9905. <https://doi.org/10.1029/2018JA025368>

- Gombosi, T. I., DeZeeuw, D. L., Groth, C. P. T., & Powell, K. G. (2000). Magnetospheric configuration for Parker-spiral IMF conditions: Results of a 3D AMR MHD simulation. *Advances in Space Research*, 26(1), 139–149. [https://doi.org/10.1016/s0273-1177\(99\)01040-6](https://doi.org/10.1016/s0273-1177(99)01040-6)
- Hosokawa, K., Miyoshi, Y., Ozaki, M., Oyama, S.-I., Ogawa, Y., Kurita, S., et al. (2020). Multiple time-scale beats in aurora: Precise orchestration via magnetospheric chorus waves. *Scientific Reports*, 10, 3380. <https://doi.org/10.1038/s41598-020-59642-8>
- Inaba, Y., Shiokawa, K., Oyama, S., Otsuka, Y., Oksanen, A., & Shinbori, A. (2020). Plasma and field observations in the magnetospheric source region of a stable auroral red (SAR) arc by the Arase satellite on 28 March 2017. *Journal of Geophysical Research: Space Physics*, 125. <https://doi.org/10.1029/2020JA028068>
- Jackel, B. J., Creutzberg, F., Donovan, E. F., & Cogger, L. L. (2003). Triangulation of auroral red-line emission heights. In K. U. Kaila, J. R. T. Jussila, & H. Holma (Eds.), *Proceedings of the 28th annual European meeting on atmospheric studies by optical methods* (pp. 97–100). Sodankyla Geophys. Observ. Publ.Oulu, Finland.
- Jones, A. V. (1974). *Aurora*. D. Reidel Publishing Co., Dordrecht, Holland.
- Karlsson, T., Andersson, L., Gillies, D.M., Lynch, K., Marghita, O., Partamias, N., & Sivadras, N., (2020). Quiet, discrete auroral arcs – observations. *Space Science Reviews*, 216, 16. <https://doi.org/10.1007/s11214-020-0641-7>
- Kozyra, J. U., & Nagy, A. F. (1997). High-altitude energy source(s) for stable auroral red arcs. *Reviews of Geophysics*, 35, 155–190. 96RG03194. <https://doi.org/10.1029/96rg03194>
- Kasaba, Y., Ishisaka, K., Kasahara, Y., Imachi, T., Yagitani, S., Kojima, H., et al. (2017). Wire probe antenna (WPT) and electric field detector (EFD) of plasma wave experiment (PWE) aboard the Arase satellite: Specifications and initial evaluation results. *Earth, Planets and Space*, 69(1), 174. <https://doi.org/10.1186/s40623-017-0760-x>
- Kasahara, S., Yokota, S., Hori, T., Keika, K., Miyoshi, Y., & Shinohara, I. (2018c). The MEP-e instrument Level-2 omni-directional flux data of Exploration of energization and Radiation in Geospace (ERG) Arase satellite. <https://doi.org/10.34515/DATA.ERG-020001>
- Kasahara, S., Yokota, S., Mitani, T., Asamura, K., Hirahara, M., Shibano, Y., & Takashima, T. (2018a). Medium-energy particle experiments-electron analyzer (MEP-e) for the exploration of energization and radiation in geospace (ERG) mission. *Earth, Planets and Space*, 70(1), 69. <https://doi.org/10.1186/s40623-018-0847-z>
- Kasahara, Y., Kasaba, Y., Kojima, H., Yagitani, S., Ishisaka, K., Kumamoto, A., et al. (2018b). The Plasma Wave Experiment (PWE) on board the Arase (ERG) satellite. *Earth, Planets and Space*, 70(1), 86. <https://doi.org/10.1186/s40623-018-0842-4>
- Kasahara, Y., Kasaba, Y., Matsuda, S., Shoji, M., Nakagawa, T., Ishisaka, K., et al. (2018d). The PWE/EFD instrument Level-2 spin-fit electric field data of Exploration of energization and Radiation in Geospace (ERG) Arase satellite. <https://doi.org/10.34515/DATA.ERG-07000>
- Kasahara, Y., Kojima, H., Matsuda, S., Ozaki, M., Yagitani, S., Shoji, M., et al. (2018f). The PWE/OFA instrument Level-2 spectrum data of Exploration of energization and Radiation in Geospace (ERG) Arase satellite. <https://doi.org/10.34515/DATA.ERG-08000>
- Kasahara, Y., Kumamoto, A., Tsuchiya, F., Matsuda, S., Shoji, M., Nakamura, S., et al. (2018e). The PWE/HFA instrument Level-2 spectrum data of Exploration of energization and Radiation in Geospace (ERG) Arase satellite. <https://doi.org/10.34515/DATA.ERG-10000>
- Kazama, Y., Wang, B. J., Wang, S. Y., Ho, P. T. P., Tam, S. W. Y., Chang, T. F., et al. (2017). Low-energy particle experiments-electron analyzer (LEPe) onboard the Arase spacecraft. *Earth, Planets and Space*, 69(1), 165. <https://doi.org/10.1186/s40623-017-0748-6>
- Keiling, A., Angelopoulos, V., Runov, A., Weygand, J., Apatenkov, S. V., Mende, S., et al. (2009). Substorm current wedge driven by plasma flow vortices: THEMIS observations. *Journal of Geophysical Research*, 114, A00C22. <https://doi.org/10.1029/2009JA014114>
- Kumamoto, A., Tsuchiya, F., Kasahara, Y., Kasaba, Y., Kojima, H., Yagitani, S., et al. (2018). High Frequency Analyzer (HFA) of Plasma Wave Experiment (PWE) onboard the Arase spacecraft. *Earth, Planets and Space*. <https://doi.org/10.1186/s40623-018-0854-0>
- Ogawa, Y., Kadokura, A., & Ejiri, M. K. (2020). Optical calibration system of NIPR for aurora and airglow observations. *Polar Science*, 26. <https://doi.org/10.1016/j.polar.2020.100570>
- Oyama, S., Shinbori, A., Ogawa, Y., Kellinsalmi, M., Raita, T., Aikio, A., et al. (2020). An ephemeral red arc appeared at 68° MLat at a pseudo-breakup during geomagnetically quiet conditions. *Journal of Geophysical Research: Space Physics*, 125, e2020JA028468. <https://doi.org/10.1029/2020JA028468>
- Ozaki, M., Miyoshi, Y., Shiokawa, K., Hosokawa, K., Oyama, S.-I., Kataoka, R., et al. (2019). Visualization of rapid electron precipitation via chorus element wave-particle interactions. *Nature Communications*, 10, 257. <https://doi.org/10.1038/s41467-018-07996-z>
- Powell, K. G., Roe, P. L., Linde, T. J., Gombosi, T. I., & De Zeeuw, D. (1999). A solution-adaptive upwind scheme for ideal magnetohydrodynamics. *Journal of Computational Physics*, 154(2), 284–309. <https://doi.org/10.1006/jcph.1999.6299>
- MacDonald, E. A., Donovan, E., Nishimura, Y., Case, N. A., Gillies, D. M., Gallardo-lacourt, B., et al. (2018). New science in plain sight: Citizen scientists lead to the discovery of optical structure in the upper atmosphere. *Science Advances*, 4(March), 16–21. <https://doi.org/10.1126/sciadv.aag0030>
- Matsuda, S., Kasahara, Y., Kojima, H., Kasaba, Y., Yagitani, S., Ozaki, M., et al. (2018). Onboard software of Plasma Wave Experiment aboard-Arased: Instrument management and signal processing of waveform capture/onboard frequency analyzer. *Earth, Planets and Space*, 70(1), 75. <https://doi.org/10.1186/s40623-018-0838-0>
- Matsuoka, A., Teramoto, M., Nomura, R., Nose, M., Fujimoto, A., Tanaka, Y., et al. (2018a). The ARASE (ERG) magnetic field investigation. *Earth, Planets and Space*, 70(1). <https://doi.org/10.1186/s40623-018-0800-1>
- Matsuoka, A., Teramoto, M., Imajo, S., Kurita, S., Miyoshi, Y., & Shinohara, I. (2018b). The MGF instrument Level-2 spinfit magnetic field data of Exploration of energization and Radiation in Geospace (ERG) Arase satellite. <https://doi.org/10.34515/DATA.ERG-060001>
- Miyoshi, Y., Shinohara, I., Takashima, T., Asamura, K., Higashio, N., Mitani, T., et al. (2018a). Geospace exploration project ERG. *Earth, Planets and Space*, 70(1), 101. <https://doi.org/10.1186/s40623-018-0862-0>
- Miyoshi, Y., Hori, T., Shoji, M., Teramoto, M., Chang, T. F., Matsuda, S., et al. (2018b). The ERG Science Center. *Earth, Planets and Space*, 70(1), 96. <https://doi.org/10.1186/s40623-018-0867-8>
- Miyoshi, Y., Shinohara, I., & Jun, C.-W. (2018c). *The Level-2 orbit data of Exploration of energization and Radiation in Geospace (ERG) Arase satellite*. <https://doi.org/10.34515/DATA.ERG-12000>
- Motoba, T., Ohtani, S., Anderson, B. J., Korth, H., Mitchell, D., Lanzerotti, L. J., et al. (2015). On the formation and origin of substorm growth phase/onset auroral arcs inferred from conjugate space-ground observations. *Journal of Geophysical Research: Space Physics*, 120, 8707–8722. <https://doi.org/10.1002/2015JA021676>
- Moshupi, M. C., Anger, C. D., Murphree, J. S., Wallis, D. D., Whitteker, J. H., & Brace, L. H. (1979). Characteristics of trough region auroral patches and detached arcs observed by Isis 2. *Journal of Geophysical Research: Space Physics*, 84(A4), 1333–1346. <https://doi.org/10.1029/JA084iA04p01333>
- Roach, F. E., & Roach, J. R. (1963). Stable 6300Å auroral arcs in midlatitudes. *Planetary Space Science*, 11, 523–545. [https://doi.org/10.1016/0032-0633\(63\)90076-x](https://doi.org/10.1016/0032-0633(63)90076-x)
- Roederer, J. G. (1970). *Dynamics of geomagnetically trapped radiation*. Cambridge Univ. Press. New York.

- Sakaguchi, K., Shiokawa, K., Miyoshi, Y., Otsuka, Y., Ogawa, T., Asamura, K., & Connors, M. (2008). Simultaneous appearance of isolated auroral arcs and Pc 1 geomagnetic pulsations at subauroral latitudes. *Journal of Geophysical Research*, *113*(A5), A05201. <https://doi.org/10.1029/2007ja012888>
- Shiokawa, K., & Fukunishi, H. (1990). Dependences of auroral 5577 Å and 6300 Å emission rates on thermosphere density variations. *Proc. NIPR Symp. Upper Atmos. Phys.*, *3*, 24–31.
- Shiokawa, K., Hosokawa, K., Sakaguchi, K., Ieda, A., Otsuka, Y., Ogawa, T., & Connors, M. (2009a). The optical mesosphere thermosphere imagers (OMTIs) for network measurements of aurora and airglow, future perspectives of space plasma and particle instrumentation and international collaborations. *AIP Conference Proceedings*, *1144*, 212–215. <https://doi.org/10.1063/1.3169292>
- Shiokawa, K., Katoh, Y., Satoh, M., Ejiri, M. K., Ogawa, T., Nakamura, T., et al. (1999). Development of optical mesosphere thermosphere imagers (OMTI). *Earth Planets Space*, *51*, 887–896. <https://doi.org/10.1186/bf03353247>
- Shiokawa, K., Otsuka, Y., & Ogawa, T. (2009b). Propagation characteristics of nighttime mesospheric and thermospheric waves observed by optical mesosphere thermosphere imagers at middle and low latitudes. *Earth Planets Space*, *61*, 479–491. <https://doi.org/10.1186/bf03353165>
- Shiokawa, K., Katoh, Y., Hamaguchi, Y., Yamamoto, Y., Adachi, T., Ozaki, M., et al. (2017). Ground-based instruments of the PWING project to investigate dynamics of the inner magnetosphere at subauroral latitudes as a part of the ERG-ground coordinated observation network. *Earth, Planets and Space*, *69*(1), 160. <https://doi.org/10.1186/s40623-017-0745-9>
- Shiokawa, K., Nose, M., Imajo, S., Tanaka, Y., Miyoshi, Y., Hosokawa, K., et al. (2020). Arase observation of the source region of auroral arcs and diffuse auroras in the inner magnetosphere. *Journal of Geophysical Research: Space Physics*, *125*, e2019JA027310. <https://doi.org/10.1029/2019JA027310>
- Shirai, H., Maezawa, K., Fujimoto, M., Mukai, T., Saito, Y., & Kaya, N. (1997). Monoenergetic ion drop-off in the inner magnetosphere. *Journal of Geophysical Research*, *102*(A9), 873–881. <https://doi.org/10.1029/97JA01150>
- Smith, P. H., & Hoffman, R. A. (1974). Direct observations in the dusk hours of the characteristics of the storm time ring current particles during the beginning of magnetic storms. *Journal of Geophysical Research*, *79*(7). <https://doi.org/10.1029/JA079i007p00966>
- Solomon, S. C., Hays, P. B., & Abreu, V. J. (1988). The auroral 6300 Å emission: Observation and modeling. *Journal of Geophysical Research*, *93*, 9867–9882. <https://doi.org/10.1029/ja093ia09p09867>
- Shepherd, G., Winningham, J., Bunn, F., & Thirkettle, F. (1980). An empirical determination of the production efficiency for auroral 6300-Å emission by energetic electrons. *Journal of Geophysical Research*, *85*(A2), 715–721. <https://doi.org/10.1029/JA085iA02p00715>
- Takagi, Y., Shiokawa, K., Otsuka, Y., Connors, M., & Schofield, I. (2018). Statistical analysis of SAR arc detachment from the main oval based on 11-year, all-sky imaging observation at Athabasca, Canada. *Geophysical Research Letters*, *45*, 11,539–11,546. <https://doi.org/10.1029/2018GL079615>
- Torr, M., & Torr, D. (1982). The role of metastable species in the thermosphere. *Reviews of Geophysics*, *20*, 91–144. <https://doi.org/10.1029/rg020i001p00091>
- Tsyganenko, N. A., & Sitnov, M. I. (2005). Modeling the dynamics of the inner magnetosphere during strong geomagnetic storms. *Journal of Geophysical Research*, *110*, A03208. <https://doi.org/10.1029/2004JA010798>
- Tóth, G., Sokolov, I. V., Gombosi, T. I., Chesney, D. R., Clauer, C., et al. (2005). Space Weather Modeling Framework: A new tool for the space science community. *Journal of Geophysical Research: Space Physics*, *110*(A12), A12226. <https://doi.org/10.1029/2005JA011126>
- Tóth, G., Sokolov, I. V., Gombosi, T. I., Chesney, C. R., Clauer, C. R., De Zeeuw, D. L., et al. (2012). Adaptive numerical algorithms in space weather modeling. Special Issue: Computational Plasma Physics. *Journal of Computational Physics*, *231*(3), 870–903. <https://doi.org/10.1016/j.jcp.2011.02.006>
- Turner, D. L., Claudepierre, S. G., Fennell, J. F., O'Brien, T. P., Blake, J. B., Lemon, C., et al. (2015). Energetic electron injections deep into the inner magnetosphere associated with substorm activity. *Geophysical Research Letters*, *42*, 2079–2087. <https://doi.org/10.1002/2015GL063225>
- Vallat, C., Ganushkina, N., Dandouras, I., Escoubet, C. P., Taylor, M. G. G. T., Laakso, H., et al. (2007). Ion multi-nose structures observed by Cluster in the inner magnetosphere. *Annales Geophysicae*, *25*, 171–190. <https://doi.org/10.5194/angeo-25-171-2007>
- Wallis, D. D., Burrows, J. R., Moshup, M. C., Anger, C. D., & Murphree, J. S. (1979). Observations of particles precipitating into detached arcs and patches equatorward of the auroral oval. *Journal of Geophysical Research*, *84*, 1347.
- Wang, S.-Y., Kazama, Y., Jun, C.-W., Chang, T.-F., Hori, T., Miyoshi, Y., & Shinohara, I. (2018). The LEPe instrument level-2 omni-directional flux data of Exploration of energization and Radiation in Geospace (ERG) Arase satellite. <https://doi.org/10.34515/DATA.ERG-04002>
- Yadav, S., Shiokawa, K., Otsuka, Y., Connors, M., & St. Maurice, J.-P. (2021). Multi-wavelength imaging observations of STEVE at Athabasca, Canada. *Journal of Geophysical Research: Space Physics*, *125*. <https://doi.org/10.1029/2020JA028622>
- Yago, K., Shiokawa, K., Hayashi, K., & Yumoto, K. (2005). Auroral particles associated with a substorm brightening arc. *Geophysical Research Letters*, *32*, L06104. <https://doi.org/10.1029/2004GL021894>
- Yokota, S., Kasahara, S., Mitani, T., Asamura, K., Hirahara, M., Takashima, T., et al. (2017). Medium-energy particle experiments-ion mass analyzer (MEP-i) onboard ERG (Arase). *Earth, Planets and Space*, *69*(1), 172. <https://doi.org/10.1186/s40623-017-0754-8>
- Yokota, S., Kasahara, S., Hori, T., Keika, K., Miyoshi, Y., & Shinohara, I. (2018). The MEP-i instrument Level-2 omni-directional flux data of Exploration of energization and Radiation in Geospace (ERG) Arase satellite. <https://doi.org/10.34515/DATA.ERG-03001>
- Zhou, S., Luan, X., Burch, J. L., Yao, Z., Han, D. S., Tian, C., et al. (2021). A possible mechanism on the detachment between a subauroral proton arc and the auroral oval. *Journal of Geophysical Research: Space Physics*, *126*, e2020JA028493. <https://doi.org/10.1029/2020JA028493>